Determination of the Atom's Excited-state Fraction in a Magneto-optical Trap

by

Yue Shen

A THESIS SUBMITTED IN PARTIAL FULFILLMENT OF
THE REQUIREMENTS FOR THE DEGREE OF

MASTER OF SCIENCE

in

The Faculty of Graduate and Postdoctoral Studies

(Physics)

THE UNIVERSITY OF BRITISH COLUMBIA

(Vancouver)

December 2018

The following individuals certify that they have read, and recommend to the Faculty of Graduate and Postdoctoral Studies for acceptance, the thesis entitled:

Determination of the Atom's Excited-state Fraction in a Magneto-optical Trap

submitted by Yue Shen in partial fulfillment of the requirements for

the degree of Master of Science

in Physics

Examining Committee:

Kirk Madison, Physics
Supervisor

James Booth, BCIT
Supervisory Committee Member

Supervisory Committee Member

Additional Examiner

Additional Supervisory Committee Members:

Supervisory Committee Member

Supervisory Committee Member

Abstract

This thesis introduces an empirical method for determining and controlling the excited-state fraction of atoms in a magneto-optical trap (MOT), which is essential for the use of cold atoms as a sensor when they are held in a MOT since their interactions with other particles and fields are quantum state dependent. A four-level theoretical atomic model was used to describe the transitions of the atoms in a MOT, and the fluorescence emitted from a fixed number of atoms under different laser conditions were measured to determine the saturation parameters empirically.

Two saturation parameters $P_{\text{sat}} = 1.15$ (0.06) mW and $P_{\text{r,sat}} = 2.05$ (0.59) mW were successfully extracted from the model, and the excited-state fraction in the four-level model was accurately calculated as a function of the MOT trap parameters, which ranges from 0.045 to 0.415 for the experimental settings currently available. We also observed minor deviations from the four-level model for the photon scattering rate, and a hypothesis of atom pinning under high powers was proposed to explain the problem. We plan to use this simple excited-state fraction determination method to distinguish the ground and excited state collision cross section of Rubidium atoms with species in residual gas of the vacuum. This is the first step to establishing atom loss rates from a MOT as an atomic primary pressure standard.

Lay Summary

This thesis introduces an empirical method for determining the fraction of atoms left in an excited state by the cooling and trapping lasers. In most cases, researchers have used the formulas derived from the simple two-level atoms interacting with a monochromatic light, which is not accurate to some extent. Thus we proposed and verified a four-level atomic model for atoms in a magneto-optical traps, predicting a more reliable value of the excited-state fraction. Such type of measurement is essential for the use of cold atoms as a sensor when they are held in a MOT since their interactions with other particles and fields are quantum state dependent.

Preface

This work is based on the experimental apparatus of Erik Frieling's undergraduate project, which is described in Section 3.1. The FPGA QDG-Bus driver system mentioned in this section was built by Wenjun Wu. I have added new magnetic coils to the MOT chamber and made the intensity stabilization system with the help of Erik Frieling. The python scripts listed in the appendix were designed by Vedangi Pathak and modified by me. All the data were collected and analyzed by myself. None of the text of the thesis is taken directly from previously published or collaborative articles.

Table of Contents

List of Tables

List of Figures

Acknowledgements

I am grateful to all those who helped me during my master's. I especially thank my supervisors, Kirk Madison and James Booth, for their patience, encouragement, and invaluable supervision to my lab work. I would also like to thank my lab colleagues Pinrui, Erik, Denis, Vedangi, Wenjun, Gene, and Will, they are so friendly and helpful. Finally, thank you to my beloved parents and friends, who have always supported me and helped me through all the difficulties.

Chapter 1

Introduction

Laser cooling has opened several exciting new chapters in atomic, molecular, and optical (AMO) physics, due to its significant advances in the research areas including improved spectroscopy, ultracold collisions [**?**] [**?**], ultracold molecule formation, quantum degenerate gases (Bose and Fermi) [**?**] [**?**], atom optics [**?**], and quantum computation [**?**]. The idea to use laser radiation to cool and trap atoms was first proposed in 1975 by Wineland and Dehmelt [**?**] and independently by Hansch and Schawlow [**?**]. The Doppler effect experienced by the moving atom renders the radiation force velocity dependent. This velocity dependence of the absorption process leads to a dissipative force which can cool the atoms down to a few microkelvins [**?**]. To compensate for the changing Doppler shift as the atoms decelerated, Zeeman slower was introduced and firstly succeeds in slowing atoms in 1982 [**?**], using a spatially varying magnetic field to tune the atomic levels along the beam path. Based on these investigations, the first magneto-optical trap (MOT) employing both optical and magnetic fields was demonstrated in 1987 [**?**]. A MOT is an essential technique in the applications of ultracold atoms, including advances in frequency metrology [**?**] [**?**], and the development of commercial cold atom instruments, such as clocks [**?**]. Due to the high sensitivity of the ultracold atoms to the interactions with their surrounding particles, ultracold atoms are also used in sensors, such as gravimeters [**?**], magnetometers [**?**], and inertial sensor [**?**].

This project investigates a primary pressure standard using the MOT. It is achieved by measuring the excited state collisions between the trapped atoms and the hot background gas particles. The background particles with high velocities run into the trapping region and collide with the trapped sensor atoms, knocking the sensor atoms out of the trapping region and thus contributing to the atom losses in the trapping field. We can measure the atom number in the MOT to devise a new pressure standard, which only relies on the long-range interaction between the trapped atom and the colliding particle. Pressure can be measured from the loss rate of atoms from a trap, Γ:

$$\Gamma = n < \sigma_{\text{loss}} v > \tag{1.1}$$

where n is the number of the background gas particles, $< \sigma_{\text{loss}} v >$ is the velocity averaged loss collision cross-section between the trapped atoms and the background particles in the vacuum system. In a magnetic trap this loss rate coeffi-

cient, $< sigma_{\text{loss}} v >$, describes collisions between ground state trapped atoms and ground state background particles. Using a MOT instead of a magnetic trap has some advantages. First, the MOT has a much larger trap depth than magnetic traps, meaning that the loss rate coefficient is much lower, allowing higher pressures to be measured. Second, the MOT is a richer environment as it contains both ground state and excited state atoms. Taking ^{87}Rb atom vapor as the test object, here Γ can be expressed as

$$\Gamma = n_{\text{Rb}} < \sigma v >_{\text{Rb+Rb}} (1 - f_{\text{e}}) + n_{\text{Rb}} < \sigma v >_{\text{Rb+Rb}^*} f_{\text{e}} + \Gamma_{\text{other}}, \tag{1.2}$$

where f_{e} is the excited-state fraction of the atoms in the MOT, and Γ_{other} is a constant rate due to other losses. The first term and the second term describe the loss rate due to collisions with the trapped atoms in their ground electronic state and their excited state, respectively. Therefore, it is necessary to differentiate these two collisions by measuring the excited-state fraction of the atoms in the MOT.

Fig. 1.1 shows the velocity-averaged collision cross section as a function of the trap depth for Argon hitting Rubidium atoms in their ground state (red circles and black squares) in a magnetic trap (MT). The prediction of what we would like to measure is plotted in the bright pink region, showing the same quantity for background Rb hitting trapped Rb atoms in their ground state (blue squares) and their excited state (pink squares). The trap depth of the Rb atoms in the MOT displayed in the bright pink region is a hundred times larger than that in the MT displayed in the bright green region.

One challenge that remains is to determine and control the excited state fraction, which is the main goal of this thesis.

Chapter 2 describes the basic theory of the physical apparatus, models, and concepts used in the experiment. The working principle of the magneto-optical trap (MOT) and its trap dynamics are introduced first. Then a two-level model and a revised four-level model are proposed to explain the atomic transitions for ^{87}Rb. The excited-state fraction is deduced and compared for the two models.

Chapter 3 contains the experimental apparatus and the experimental procedure. The apparatus includes the controlling system for the measurement, the optical setups which provide the MOT lasers, and the MOT. In the procedure section, the measuring method of the MOT fluorescence is presented.

Chapter 4 discusses the result of the experiment, determining the amount of the frequency shift for the pump laser and verifying the prediction of the four-level atomic model. The calculation of the excited-state fraction is also involved in this chapter.

Finally, Chapter 5 is a conclusion of the experimental result, which points out the next steps for establishing an atomic primary pressure standard.

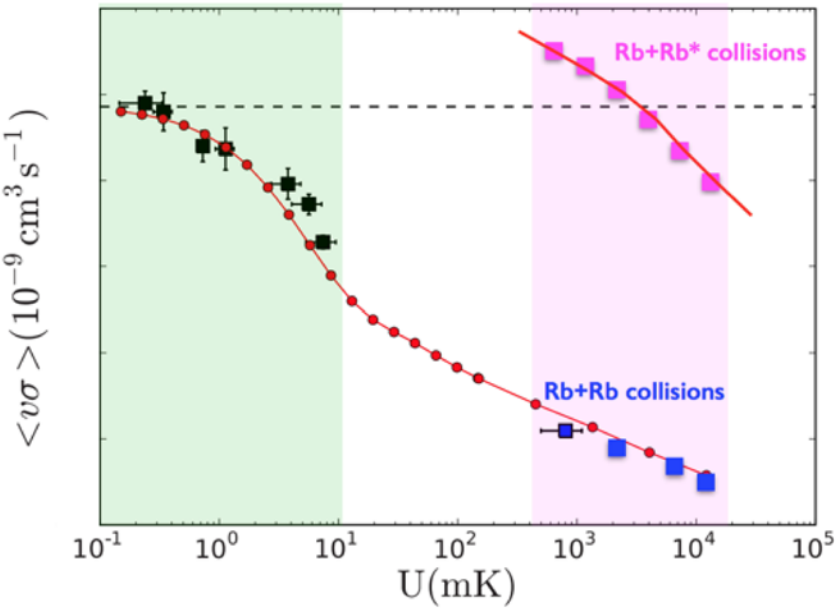

Figure 1.1: A plot of the loss inducing collision cross sections between Ar and trapped ground-state Rb atoms. This figure is plotted by my supervisor Professor Kirk Madison. The proposed measurements for background Rb hitting Rb atoms in their ground state and their excited state in the MOT are predicted in the figure and labelled by blue squares and pink squares, respectively.

Chapter 2

Theory

This chapter describes the fundamental theory in the determination of the excited-state fraction of atoms in a magneto-optical trap (MOT). It involves the principles of the MOT and its trapping dynamics, the estimates of the photon scattering rate where a four-level model is constructed to describe the cycling transitions of atoms, and the determination of the atomic excited-state fraction in the MOT.

2.1 Magneto-Optical Traps

A magneto-optical trap (MOT) is an apparatus that uses 3 pairs of counter-propagating laser beams crossing at the zero of an applied magnetic quadrupole field to capture and cool atoms to temperatures less than one millikelvin (see Fig. 2.1). The atoms in the MOT are cooled by a velocity-dependent force generated from the mechanism of Doppler effect, and trapped by a position-dependent force exploited by the Zeeman effect [**?**].

2.1.1 Doppler Cooling

Doppler cooling is a technique for laser cooling of small particles, the basic idea is that absorption and subsequent spontaneous emission of photons lead to light cooling forces, which are velocity-dependent through the Doppler effect.

To describe the motion of the atoms in a MOT, the radiative force in the low intensity limit ($I < I_{\text{sat}}$ so that stimulated emission is not important) is considered, the expression of the force from one of the counter-propagating laser beams on the atoms is given by [**?**]:

$$\vec{F}_{\pm} = \pm \left(\frac{\hbar \vec{k} \gamma}{2} \right) \left[\frac{s}{1 + s + (2\delta_{\pm}/\gamma)^2} \right], \tag{2.1}$$

where γ is the decay rate of the excited state atoms in the MOT, $\mathrm{s} = I/I_{\text{sat}}$ is a saturation parameter, and $\delta_{\pm}$ is an effective detuning of the moving atom in the light field with wave vector $\vec{k}$ and detuning δ from resonance. If an atom is travelling at a

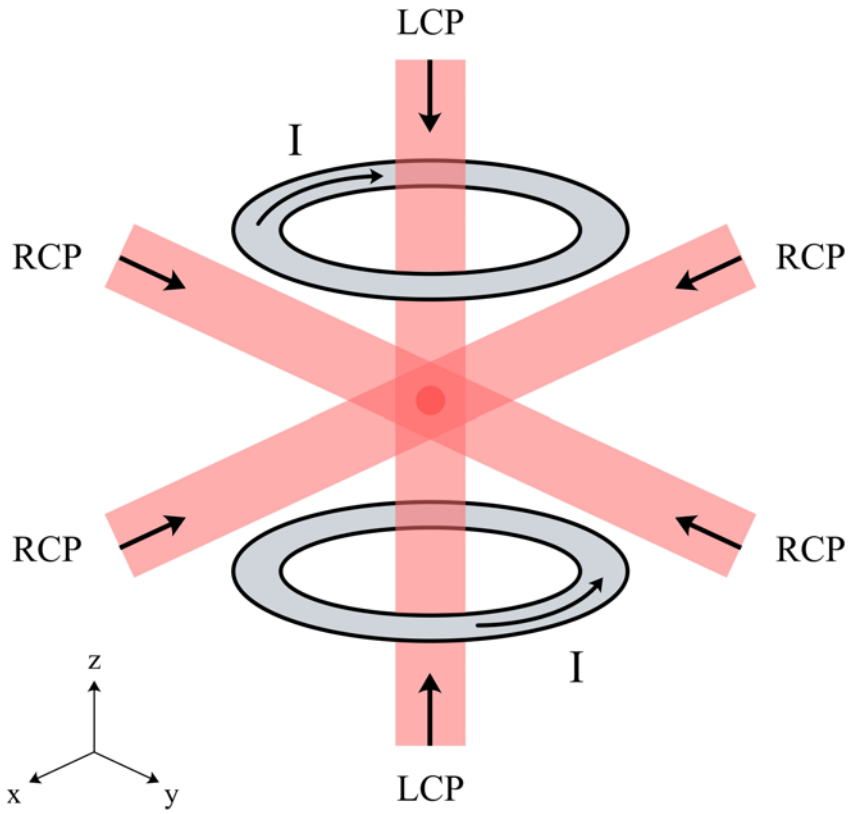

Figure 2.1: A diagram of the magneto-optical trap. Three orthogonal counter-propagating pairs of laser beams along three orthogonal spatial axes get crossed at the zero of a magnetic quadrupole field generated by a pair of anti-Helmholtz coils. The laser beams in the radial direction (in the x and y axes) are right circularly polarized (RCP), as the magnetic field opposites the direction of the laser beams. Also, the vertical beam gets left circularly polarized (LCP), where the magnetic field points towards the center of the MOT along the z axis. A MOT is generated in the crossing region from this optical molasses configuration with an applied magnetic quadrupole field.

velocity $\vec{v}$, the detuning $\delta_{\pm}$ entering in the expression of the force is Doppler shifted:

$$\delta_{\pm} = \delta \mp \vec{k} \cdot \vec{v}. \tag{2.2}$$

Then the total force of a pair of counter-propagating laser beams can be composed as [**?**]

$$\begin{aligned} \vec{F} &= \vec{F}_{+} + \vec{F}_{-} \\ &\cong \frac{8\hbar k^2 \delta s \vec{v}}{\gamma[1 + s + (2\delta/\gamma)^2]} \equiv \beta \vec{v}. \end{aligned} \tag{2.3}$$

This is a dissipative force proportional to velocity with a damping coefficient β. If a laser is detuned below the atomic resonance frequency, that is $\delta < 0$, the atoms experience a damping force opposing their velocities. By using three intersecting orthogonal pairs of oppositely directed beams, the movement of atoms in the beam overlap volume is damped, slowing the atoms and creating an "optical molasses".

In principle, the atoms' velocity should be reduced to zero very quickly, resulting in a temperature of T = 0 K. However, one should also consider some heating caused by the light beams, due to the discrete size of the momentum steps the atoms undergo with each emission or absorption [**?**]. The competition between this heating with the damping force results in a nonzero kinetic energy in the steady state. The temperature is found by equating the average energy imparted per scattered photon to the atom:

$$T_{\mathrm{D}} = \frac{\hbar\gamma}{2k_{\mathrm{B}}}, \tag{2.4}$$

where k_{B} is Boltzmann constant and T_{D} is called the Doppler temperature [**?**]. For the D_2 transition of ^{87}Rb, this temperature is equal to 145 μK, which gives an estimates of the ensemble energy in our experiment.

2.1.2 Magnetic Field

Doppler cooling rapidly slows down the atoms in the intersection volume of the laser beams, but the cold atoms are not trapped and will eventually diffuse out of the cooling region.. In order to trap atoms, a position-dependent force must be introduced. A quadrupolar magnetic field superimposed on the molasses achieves this.

The magnetic quadrupole field is produced by a pair of coils in anti-Helmholtz configuration, where two identical concentric coils are shifted vertically and carrying the same current in opposite directions. Fig. 2.2 describes that this magnetic field goes to zero at the center between the coils and increases linearly in magnitude away from the center. The magnetic field points outwards away from the center along the radial direction, and points toward the center of the MOT along the

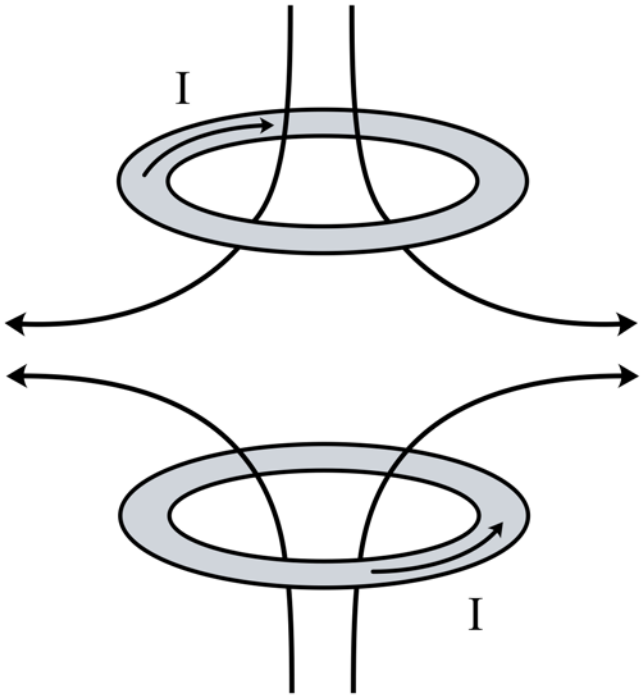

Figure 2.2: A diagram of magnetic field lines generated by a pair of coils in anti-Helmholtz configuration, where the current in the coils is circulating in opposite directions. The magnetic field is zero at the center between the coils and increases linearly in magnitude away from the center, pointing outwards from the center along the radial direction and towards the center in the axial direction.

axial direction. For a spherical quadrupole configuration, the axial field gradient, $d|\vec{B}_z|/dz$, is twice the radial field gradient, $d|\vec{B}_\rho|/d\rho$.

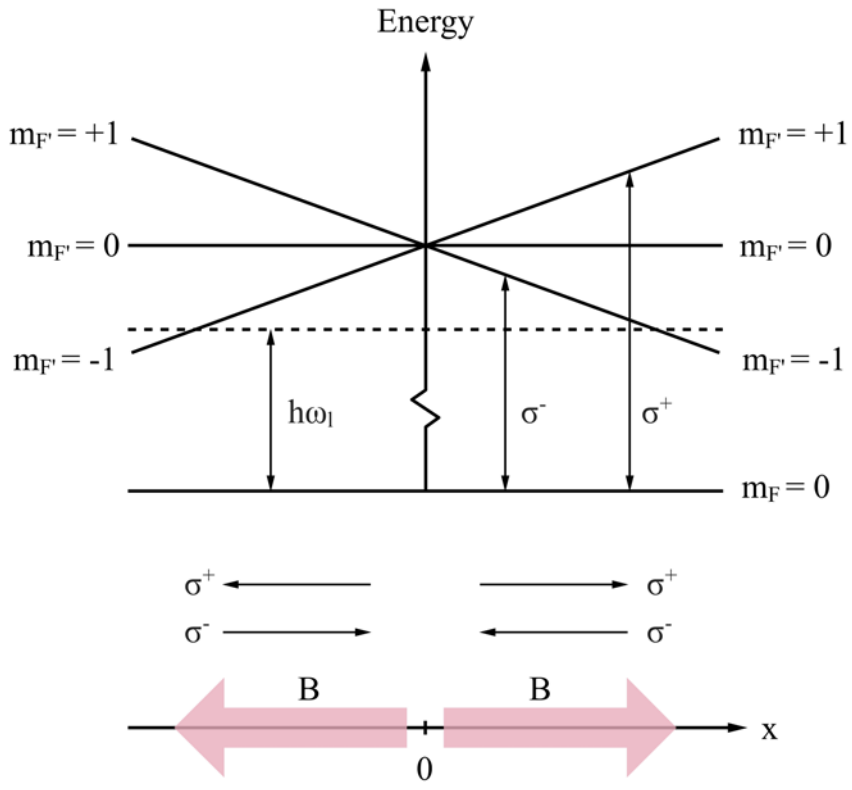

Figure 2.3: Principle of a MOT in 1D. The energy of the hyperfine sublevels is linearly shifting with the changing magnetic field because of the Zeeman effect. The $m_F = 0 \rightarrow m_{F'} = -1$ transition (σ^-) is closest to the laser frequency labelled by the horizontal dashed line. Therefore, atoms not at the center of the trap prefer to resonance with the σ^- laser beam and are pushed towards the zero of the magnetic field at x = 0.

By the optical pumping of slowly moving atoms in this magnetic field, the atoms are confined close to the zero of the magnetic field. A simple 1D scheme of the atomic transitions with three Zeeman components can explain the mechanism (see Fig. 2.3), where a laser light with energy $h\omega_l$ is detuned below the zero field atomic resonance. When the atoms move in a weak magnetic field $\vec{B}$ generated in a MOT, the potential energy they experience for different hyperfine state

magnetic sub-levels m_F is

$$U = g_F m_F \mu_B |\vec{B}|, \tag{2.5}$$

where g_F is the Landé g-factor, and μ_B is the Bohr magneton. Therefore the excited state $m_{F'} = +1$ is shifted up for $g_{F'}>0$, whereas the state with $m_{F'}$ = -1 is shifted down, because of the Zeeman shift. In Fig. 2.3, the transition of $m_F = 0 \rightarrow m_{F'} = -1$ (σ^-) is tuned closer to the laser frequency than the $m_F = 0 \rightarrow m_{F'} = +1$ (σ^+) transition, so the atoms will absorb more light from the σ^- beam. To push the atoms towards the center of the trap where the magnetic field is zero, the polarization of the laser beam incident from the same direction as the magnetic field is chosen to be σ^+, which is right circularly polarized, and correspondingly σ^- for the other beam counter propagating with respect to the B-field direction. In the z axis, B-field is pointing towards the center of the trap, the polarization of the laser light should be reversed (that is left circularly polarized), then the laser in z axis incident inwards the center also drives the σ^- transitions. As a result, the atoms preferentially absorb light that drives them to the zero of a magnetic field, which is the center of the MOT.

2.1.3 Trap Dynamics

The dynamics of MOT loading and loss can be modeled from the rate equation

$$\dot{N} = R - \Gamma N - \beta \int n^2(\vec{r}, t) d^3\vec{r}. \tag{2.6}$$

Here N is the number of atoms in the MOT, t = 0 is the time when both the magnetic field and the light are turned on and the MOT starts loading, and $\vec{r} = 0$ means the center of the MOT. The first term in the equation is the loading rate, R, which describes the loading of atoms from the background vapor. It is directly proportional to the background atoms' density and the square of the trap depth [**?**]. The trap losses are described by Γ, the rate constant for losses due to collisions between the trapped atoms and the hot background gases. The third term describes two body intra-trap losses, $\beta \int n^2(\vec{r}, t)$ describes the losses due to radiative escape, fine-structure collisions, hyperfine collisions, and intra-trap collisions, where β is the rate constant for losses due to inelastic two-body collisions within the trap, and $n(\vec{r}, t)$ is the density of the atoms in the trap.

K. R. Overstreet et al [**?**] pointed out that the trapped atoms are confined in a space with constant volume for a MOT with atom number N less than of order 10^5, since the repulsive interactions from light scattering between atoms are weak and negligible in this regime. For a MOT with constant volume, the density of the trapped atoms is modeled as

$$n(\vec{r}, t) = n_0(t) e^{-(\frac{r}{a})^2}, \tag{2.7}$$

where $n_0(t)$ is the peak density of the MOT when $\vec{r} = 0$, and a is a constant. Thus the solution to Eq. (2.6) is [**?**]

$$N(t) = N_{ss}\left(\frac{1 - e^{-\gamma t}}{1 + \chi e^{-\gamma t}}\right). \tag{2.8}$$

Here $\gamma = \Gamma + 2\beta n_{ss}$ and $\chi = \beta n_{ss}/(\Gamma + \beta n_{ss})$, n_{ss} is the average steady-state density of the MOT expressed by

$$n_{ss} = \left(\frac{\int n^2 d^3 r}{\int n d^3 r}\right)_{ss}. \tag{2.9}$$

In addition, the steady-state MOT number N_{ss} should follow

$$N_{ss} = \frac{R}{\Gamma + \beta n_{ss}}. \tag{2.10}$$

In the limit where $\Gamma \gg \beta n_{ss}$, Eq. (2.8) simplifies:

$$N(t) = \frac{R}{\Gamma}(1 - e^{-\Gamma t}). \tag{2.11}$$

For larger N, the relative significance of the two-body losses is reduced. Light scattering leads to a constant mean density of the trapped atoms, $\overline{n}$, with the MOT growing in volume with the increasing atom number. The mean density $\overline{n}$ is defined as $\overline{n} = (1/N)\int n^2(\vec{r}, t) d^3\vec{r}$. In the constant density limit, the solution to Eq. (2.6) is [**?**]

$$N(t) = \frac{R}{\Gamma + \beta\overline{n}}\left(1 - e^{-\overline{\gamma} t}\right), \tag{2.12}$$

where $\overline{\gamma} = \Gamma + \beta\overline{n}$. If $\Gamma \gg \beta\overline{n}$, this solution has the same form as Eq. (2.11).

2.2 Photon Scattering Rate

The estimate of the photon scattering rate is quite useful in the calculations of the number of atoms in the MOT and the excited-state fraction. In most cases, a standard two-level model is utilized to determine this value, with the saturation intensity corresponding to the $F = 2 \rightarrow F = 3'$ pump cycling transition while ignoring the scattering from any light tuned to the $F = 1 \rightarrow F = 2'$ repump transition. To produce a more accurate photon scattering rate, the hyperfine pumping effects are considered in a four-level atomic transition model, and an experimental parameter G is measured using the fluorescence emitted from a fixed number of atoms under different conditions.

2.2.1 Two-Level Model

In our experiment, a pump beam transfers atoms in the $|F, m_F\rangle = |2, 2\rangle$ to the $|F', m_{F'}\rangle = |3, 3\rangle$ state of the D_2 ($5^2S_{1/2} \rightarrow 5^2P_{3/2}$) manifold transitions for ^{87}Rb. The steady-state photon scattering rate per atom for a two-level atomic model, γ_{sc}, can be derived using the density matrix approach as [**?**]:

$$\gamma_{sc} = \frac{\gamma}{2} \frac{s}{1 + s + (2\Delta/\gamma)^2}, \tag{2.13}$$

where γ is the natural decay rate of the atoms in the excited states, and Δ is the pump laser detuning, which is the difference between the laser's optical frequency and the resonance frequency of the F = 2 → F' = 3 pump transition. Here $s = I/I_{sat}$, where I is the intensity of the pump laser light experienced by the trapped atoms, and I_{sat} is the saturation intensity of the pump transition, which is the intensity needed for a beam to excite the pump transition at a rate equal to one half of its natural line width. To investigate the behaviour of the atoms in the experiment, we focus the fluorescent light signal, which is emitted from the cold atoms in the MOT, on a photodetector. The converted electrical signal, V_{fluo}, can be expressed as

$$V_{fluo} = \alpha \gamma_{sc} N, \tag{2.14}$$

where α is the photon collection efficiency of the optical system times the photon-to-voltage conversion factor for the detector, and N is the number of atoms that emits photons. This equation is under the condition that each photon is only scattered from a single atom before leaving the dilute MOT.

If we assume that the laser power measured outside the MOT, P, is proportional to the intensity of the laser light on the MOT, I, the parameter s in Eq. (2.13) becomes $s = I/I_{sat} = P/P_{sat}$. P_{sat} is a strictly experimentally determined parameter, simplifying the measurement procedure. That is, it is impossible to measure I_{sat} at the location of the MOT. Thus, we choose to measure P at a convenient location outside the vacuum cell and P_{sat} the corresponding experimental parameter used to estimate s. Therefore, P and Δ are the parameters that can be controlled precisely in the experiment. By contrast α and N are difficult to measure precisely, so the experimental method described here removes them from the measurements. With the hypothesis that Eq. (2.14) is a good approximation for the experiment, the MOT is loaded to equilibrium under some pre-determined laser settings (power, detuning), then the settings are quickly switched to a set of "standard" settings. As computed in Eq. (2.14), the theoretical ratio of the steady-state MOT fluorescence at the test parameter settings, V, to the steady-state MOT fluorescence using the "standard"

settings, V_{std}, is

$$\begin{aligned}\frac{V_{\mathrm{std}}}{V} = \frac{\gamma_{\mathrm{sc}}^{\mathrm{std}}}{\gamma_{\mathrm{sc}}} &= \frac{s_{\mathrm{std}}}{s}\frac{1+s+(2\Delta/\gamma)^2}{1+s_{\mathrm{std}}+(2\Delta_{\mathrm{std}}/\gamma)^2} \\ &= \frac{P_{\mathrm{std}}}{P}\frac{1}{\xi_{\mathrm{std}}^{(2)}}\left(A+\frac{P}{P_{\mathrm{sat}}}\right),\end{aligned} \tag{2.15}$$

where the switching time (<300 μs) is short compared to the time for N to change so that N is constant for it to cancel out. The detuning-dependent quantity $A = 1+(2\Delta/\gamma)^2$ is defined here for convenience. The term $\xi_{\mathrm{std}}^{(2)} = A_{\mathrm{std}}+s_{\mathrm{std}}$ is a common scaling factor determined by the standard laser beam settings s_{std} and Δ_{std}, which are constant values as the laser standard settings are fixed.

Eliminating the ratio of standard and test powers from the signal ratio in Eq. 2.15, one finally obtains:

$$G_2 = \left(\frac{P}{P_{\mathrm{std}}}\right)\left(\frac{V_{\mathrm{std}}}{V}\right) = \frac{1}{\xi_{\mathrm{std}}^{(2)}}\left(A+\frac{P}{P_{\mathrm{sat}}}\right). \tag{2.16}$$

G is an experimental parameter constructed from four easily measured quantities P, P_{std}, V, and V_{std}, which provides a method to determine the pump saturation power by fitting experimentally determined values of G to the model. For a fixed pump detuning Δ, the relation in Eq. (2.16) from the two-level atom model shows a linear relationship between the empirical parameter G and the pump power P. The deduced slope $m_{\mathrm{G}}^{(2)}$ is

$$m_{\mathrm{G}}^{(2)} = \frac{1}{\xi_{\mathrm{std}}^{(2)}}\frac{1}{P_{\mathrm{sat}}}, \tag{2.17}$$

and the intercept $b_{\mathrm{G}}^{(2)}$ is

$$b_{\mathrm{G}}^{(2)} = \frac{1}{\xi_{\mathrm{std}}^{(2)}}A. \tag{2.18}$$

Combining theses two quantities, one can determine P_{sat} from the two-level model:

$$P_{\mathrm{sat}} = \frac{b_{\mathrm{G}}^{(2)}}{m_{\mathrm{G}}^{(2)}A} \tag{2.19}$$

2.2.2 Four-Level Model

A limitation of the two-level model is that it does not describe the fact that the pump light also non-resonantly excites transitions from ground state F = 2 to the

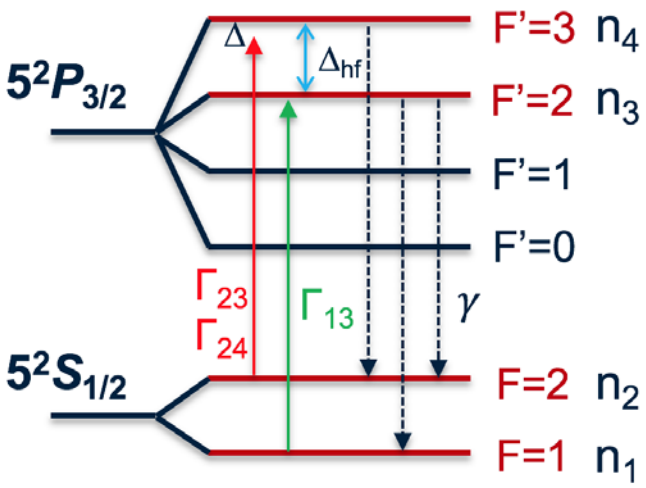

Figure 2.4: A schematic diagram of the four-level model for the atoms of ^{87}Rb. n_1, n_2, n_3, and n_4 represent four levels with increasing energy. Δ is the pump laser detuning from the $F = 2 \rightarrow F = 3'$ pump transition; and Δ_{hf} is the energy difference between the $F = 2'$ and $F = 3'$ hyperfine atomic levels.

hyperfine state F' = 2. The excited atoms in this state then decay to the F = 1 and F = 2 state. In particular, atoms ending in the F = 1 ground state can not form a cycling transition, requiring the addition of a repump laser. Therefore, the effect of the repump light has to be added to the model. The repump laser resonantly excites atoms from the F = 1 to the F' = 2 state, and finally leads to a decay of the atoms back to the F = 2 state, due to spontaneous emission, at a rate γ. The D_2 transition ($5^2S_{1/2} \rightarrow 5^2P_{3/2}$) for ^{87}Rb has $\gamma = (2\pi)6.065(9)$ MHz, and the energy difference between the $F = 2'$ and $F = 3'$ hyperfine atomic levels, Δ_{hf}, is equal to 266.650(9) MHz [**?**].

For this cycling transition, a four-level atom model is constructed to describe the atoms of ^{87}Rb as if they were confined to 4 states. Fig. 2.4 shows the schematic diagram, where n_1, n_2, n_3, and n_4 refer to the states $F = 1$, $F = 2$, $F = 2'$, and $F = 3'$ respectively. Atoms in n_1, n_2, n_3, and n_4 states can be described by the following couple rate equations:

$$\begin{aligned}
\dot{n}_1 &= -\Gamma_{13}n_1 + (\Gamma_{13} + \gamma/2)n_3, \\
\dot{n}_2 &= -\Gamma_{23}n_2 - \Gamma_{24}n_2 + (\Gamma_{23} + \gamma/2)n_3 + (\Gamma_{24} + \gamma)n_4, \\
\dot{n}_3 &= \Gamma_{13}n_1 + \Gamma_{23}n_2 - (\Gamma_{13} + \Gamma_{23} + \gamma)n_3, \\
\dot{n}_4 &= \Gamma_{24}n_2 - (\Gamma_{24} + \gamma)n_4,
\end{aligned} \tag{2.20}$$

with Γ_{ij} representing the rate at which atoms are excited from levels n_i to n_j. In equilibrium $\dot{n}_i = 0$, and the total atom number $N = \sum_i n_i$ is conserved. Solving the rate equations in steady state where the derivatives vanish one obtains the steady state populations of the F' = 2 (n_3) and F' = 3 (n_4) atomic hyperfine levels,

$$\begin{aligned}
n_3 &= \left(\frac{2\Gamma_{23}/\gamma}{1 + 2\Gamma_{23}/\gamma}\right)\left(\frac{N}{D}\right), \\
n_4 &= \left(\frac{\Gamma_{24}/\gamma}{1 + \Gamma_{24}/\gamma}\right)\left(\frac{N}{D}\right),
\end{aligned} \tag{2.21}$$

where D is a quantity defined by

$$D = 1 + \left(\frac{2\Gamma_{23}/\gamma}{1 + 2\Gamma_{23}/\gamma}\right)\left(\frac{1 + 4\Gamma_{13}/\gamma}{2\Gamma_{13}/\gamma}\right) + \frac{\Gamma_{24}/\gamma}{1 + \Gamma_{24}/\gamma}. \tag{2.22}$$

The measured voltage of the fluorescence due to the photons emitted by the excited-state atoms is calculated from Eq. (2.14) as

$$\begin{aligned}
V &= \alpha\gamma(n_3 + n_4) \\
&= \alpha\gamma\left(\frac{2\Gamma_{23}/\gamma}{1 + 2\Gamma_{23}/\gamma} + \frac{\Gamma_{24}/\gamma}{1 + \Gamma_{24}/\gamma}\right)\left(\frac{N}{D}\right).
\end{aligned} \tag{2.23}$$

And the atom's transition rate Γ_{ij} can be expressed from Budker's book [**?**]:

$$\begin{aligned}
\Gamma_{13} &= \left(\frac{\gamma}{2}\right)\left(\frac{I_r}{I_{sat}^{1-2'}}\right) = \frac{\gamma}{2}s_r, \\
\Gamma_{24} &= \left(\frac{\gamma}{2}\right)\left(\frac{I}{I_{sat}^{2-3'}}\right)\left[\frac{1}{1+\left(\frac{2\Delta}{\gamma}\right)^2}\right] = \frac{\gamma}{2}\frac{s}{A}, \\
\Gamma_{23} &= \left(\frac{\gamma}{2}\right)\left(\frac{I}{I_{sat}^{2-2'}}\right)\left[\frac{1}{1+\left(\frac{2(\Delta+\Delta_{hf})}{\gamma}\right)^2}\right] = \frac{\gamma}{2}\frac{\epsilon s}{B}.
\end{aligned} \tag{2.24}$$

Here $I_{sat}^{2-3'} = I_{sat}$, $I_{sat}^{1-2'} = I_{r,sat}$, and $I_{sat}^{2-2'}$ are the saturation intensities for the pump transition ($F = 2 \rightarrow F = 3'$), repump transition ($F = 1 \rightarrow F = 2'$), and the non-resonant transition ($F = 2 \rightarrow F = 2'$), respectively. The two detuning-dependent quantities $A = 1 + (2\Delta/\gamma)^2$ and $B = 1 + [2(\Delta + \Delta_{hf})/\gamma]^2$ are defined here for simpler notation. ϵ is assigned to be the ratio of the saturation intensity for the $F = 2 \rightarrow F = 3'$ pump transition, $I_{sat}^{2-3'}$, to the saturation intensity for the $F = 2 \rightarrow F = 2'$ transition, $I_{sat}^{2-2'}$. It has a value $\epsilon = I_{sat}^{2-3'}/I_{sat}^{2-2'} = 3.577/10.01 = 0.3572$ in this situation [**?**].

Combining Eq. (2.22), Eq. (2.23), and Eq. (2.24), the fluorescence signal detected from the photodetector is

$$V = \alpha\gamma N\left[\frac{s}{2(A+s)}\right]\left(\frac{H}{W}\right) \tag{2.25}$$

with

$$\begin{aligned}
H &= \frac{B + 2\epsilon(A+s)}{B+\epsilon s}, \\
W &= 1 + \left(\frac{k_r \epsilon s}{B+\epsilon s}\right)\left(\frac{A+s/2}{A+s}\right).
\end{aligned} \tag{2.26}$$

To characterizes the effect of the repump laser on the observed fluorescence, the factor k_r is introduced, which provides the method to determine the repump saturation power. Its definition is

$$k_r = 2 + \frac{I_{r,sat}}{I_r} = 2 + \frac{P_{r,sat}}{P_r}, \tag{2.27}$$

Using the same ratio-metric method as in the two level model, one can construct

the four-level empirical parameter G_4 as

$$\begin{aligned} G_4 &= \left(\frac{P}{P_{\text{std}}}\right)\left(\frac{V_{\text{std}}}{V}\right) \\ &= \left(\frac{1}{A_{\text{std}}+s_{\text{std}}}\right)\left(\frac{H_{\text{std}}}{W_{\text{std}}}\right)(A+s)\left(\frac{W}{H}\right) \\ &= \frac{1}{\xi^{(2)}_{\text{std}}}\left(\frac{H_{\text{std}}}{W_{\text{std}}}\right)(A+s)\left(\frac{W}{H}\right) \end{aligned} \tag{2.28}$$

For a two-level model, the factor B goes to infinity, which leads to $H \to 1$ and $W \to 1$. Therefore Eq. (2.28) reduces to the two-level parameter $G_2 = (1/\xi^{(2)}_{\text{std}})(A+s)$.

Estimates of Saturation Parameters

For the four-level atomic model, the expansion equation for G_4 is complicated:

$$\begin{aligned} G_4 &= \left(\frac{1}{A_{\text{std}+s_{\text{std}}}}\cdot\frac{H_{\text{std}}}{W_{\text{std}}}\right)\left[\frac{\epsilon s^2(1+k_{\text{r}}/2)+s[B+\epsilon(1+k_{\text{r}})A]+AB}{B+2\epsilon(A+s)}\right] \\ &= \frac{1}{\xi^{(4)}_{\text{std}}}\left[\frac{\epsilon s^2(1+k_{\text{r}}/2)+s[B+\epsilon(1+k_{\text{r}})A]+AB}{B+2\epsilon(A+s)}\right] \end{aligned} \tag{2.29}$$

Eq. (2.29) simplifies considerably in the case studied in the thesis where the detuning Δ is much smaller than the hyperfine splitting in the excited state and s is not huge. It can be motivated by estimating the values of the parameters achieved in the experiment. First, we need to estimate the theoretical values of P_{sat} and $P_{\text{r,sat}}$. C. Gabbanini *et al*. [**?**] pointed that one should calculate an average over all the transitions between the various Zeeman sublevels in the ground and excited states to include the effects of partial optical pumping of the atoms in the MOT. Thus an averaged squares of the Clebsch-Gordan coefficients C^2 should be used to weight the pump saturation parameter s in the scattering rate calculations, which is equal to 0.46 for ^{87}Rb. It is also stated that there is an uncertainty $\delta(C^2)/(C^2) = 25\%$ for a cesium MOT [**?**]. Moreover, the laser beam loses intensity when passing through the MOT apparatus so a factor η (90%) is multiplied for the laser intensity after the transmission; passes through the vapor cell sides also decrease the intensity of the MOT beams, the efficiency at each window is β (90%).

Hence a better description of the saturation parameter s is

$$s = \frac{I}{I_{\text{sat}}} = \frac{C^2 a I}{I_{\text{sat}}}. \tag{2.30}$$

Here $a = \eta\beta(1+\beta^2)/2$, the terms β and β^3 are owing to the incoming and the retroreflected beams in the MOT configuration, respectively. The intensity of the laser beam measured outside the vacuum cell in Eq. (2.30) can be expressed as [**?**]:

$$I = \frac{2P}{\pi w^2}, \tag{2.31}$$

where w is the $1/e^2$ radius of the beam. Combining Eq. (2.30) and Eq. (2.31), and recall the assumption that $I/I_{\text{sat}} = P/P_{\text{sat}}$, one can thus deduce the estimation of P_{sat} from the known I_{sat} value:

$$P_{\text{sat}} = \frac{\pi w^2 I_{\text{sat}}}{2C^2 a} \tag{2.32}$$

To calculate this value, the diameter of the beam circle with 95% power transmitted through it, D_i, was measured, and the $1/e^2$ beam radius can be computed from $w_{\text{i}} = D_{\text{i}}/(2 \times 1.224)$ [**?**]. For the two horizontal beams paralleled to the MOT table, the diameter of the laser beam is 1.03 cm, and for the beam vertically passing the MOT cell, the diameter is 0.95 cm. Using $I_{\text{sat}} = 3.577$ mW cm^{-2} [**?**], the value of P_{sat} can be estimated from Eq. (2.32) to be $P_{\text{sat}} = 1.994$ mW. Similarly, the estimated value of $P_{\text{r,sat}}$ is 3.351 mW, knowing that the theoretical repump saturation intensity $I_{\text{r,sat}} = 6.01$ mW cm^{-2} [**?**]. However, these estimates have large uncertainties, owing to the uncertainties in the beam widths (5 %), the transmission losses through the MOT apparatus as well as the glass cells, and the uncertainty of the coefficient C^2 (25 %). Consequently, the estimates of the lasers' saturation powers are $P_{\text{sat}} = 1.99$ (0.74) mW and $P_{\text{r,sat}} = 3.35$ (1.25) mW.

	Pump Laser		Repump Laser	
	Power (mW)	Detuning (MHz)	Power (mW)	Detuning (MHz)
Standard Settings	18	-10	0.483	0
Test Settings	7 to 28	-6 to -14	0.011 to o.483	0

Table 2.1: Standard and test settings applied in the measurement for the lasers.

Secondly, we can study the settings used in the experiment. For standard settings, the pump laser gives a total power of 18 mW to the MOT ($P_{\text{std}} = 18$ mW) and is red detuned by 10 MHz from the $F = 2 \rightarrow F' = 3$ pump transition ($\Delta_{\text{std}} =$ -10 MHz); while the full repump power going into the cell is 0.483 mW ($P_{\text{r,std}} =$ 0.483 mW), and is resonant with the repump transition $F = 1 \rightarrow F = 2'$ ($\Delta_{\text{r,std}} =$ 0 MHz). For test settings, the pump power P is varied from 7 mW to 28 mW with the detuning Δ range from -6 to -14 MHz, and the repump detuning is kept zero. The values of the laser settings are reported in Table. 2.1.

Therefore one expects:

- $5 < A < 22$, $A_{\text{std}} \approx 11$.
- $6900 < B < 7400$, $B_{\text{std}} \approx 7200$.
- $s < 100$, $s_{\text{std}} \approx 9$.
- $k_{\text{r}} = 2$ for $P_{\text{r}} \to \infty$, $k_{\text{r}} = \infty$ for $P_{\text{r}} \to 0$. $k_{\text{r,std}} \approx 9$

G Simplification

Using the estimated parameters in section 2.2.3, one obtains that in the denominator of G_4 in Eq. (2.29), $B \gg 2\epsilon(A+s)$, the denominator $[B + 2\epsilon/(A+s)]$ can be expanded as

$$\begin{aligned}\frac{1}{B+2\epsilon(A+s)} &\approx \frac{1}{B}\left[1 - \frac{2\epsilon(A+s)}{B} + \frac{4\epsilon^2(A+s)^2}{B^2} - \frac{8\epsilon^3(A+s)^3}{B^3} + \dots\right] \\ &\approx \frac{1}{B}\left[1 - \frac{2\epsilon A}{B} - \frac{2\epsilon s}{B} + \frac{4\epsilon^2 A^2}{B^2} + \frac{8\epsilon^2 sA}{B^2} + \frac{4\epsilon^2 s^2}{B^2} - \frac{8\epsilon^3 A^3}{B^3}\right. \\ &\quad \left. - \frac{24\epsilon^3 sA^2}{B^3} - \frac{24\epsilon^3 s^2 A}{B^3} - \frac{8\epsilon^3 s^3}{B^3} + \dots\right].\end{aligned} \tag{2.33}$$

Due the the fact that A/B ≈ 0.002, we only keep the terms up to order A/B in the function, thus the parameter G_4 from the four-level model is estimated as follows:

$$\begin{aligned}G_4 &= \left(\frac{P}{P_{\text{std}}}\right)\left(\frac{V_{\text{std}}}{V}\right) \\ &= \left(\frac{1}{\xi^{(4)}_{\text{std}}}\right)\cdot\left[A\left(1 - 2\epsilon\frac{A}{B}\right) + s\left(1 + \epsilon(k_{\text{r}} - 3)\frac{A}{B}\right)\right. \\ &\quad \left. + \frac{\epsilon s^2}{B}\left(\frac{1}{2}(k_{\text{r}} - 2) - \epsilon(3k_{\text{r}} - 4)\frac{A}{B}\right)\right].\end{aligned} \tag{2.34}$$

Because of the parameter B in the denominator of the quadratic coefficient in Eq. (2.34), it can be concluded that the term quadratic in s^2 is much smaller than the other two terms. It can also be proved by the linearity in Fig. 2.5, where G is plotted as a function of s, using the standard values of Δ, P_{r} and the estimated values of P_{sat}, $P_{\text{r,sat}}$. Therefore, the third term in Eq. (2.34) can be neglected from the equation. Finally we have the result of the simplified equation of G in a four-level atom model:

$$G = \left(\frac{1}{\xi^{(4)}_{\text{std}}}\right)\left[A\left(1 - 2\epsilon\frac{A}{B}\right) + \frac{P}{P_{\text{sat}}}\left(1 + \epsilon(k_{\text{r}} - 3)\frac{A}{B}\right)\right]. \tag{2.35}$$

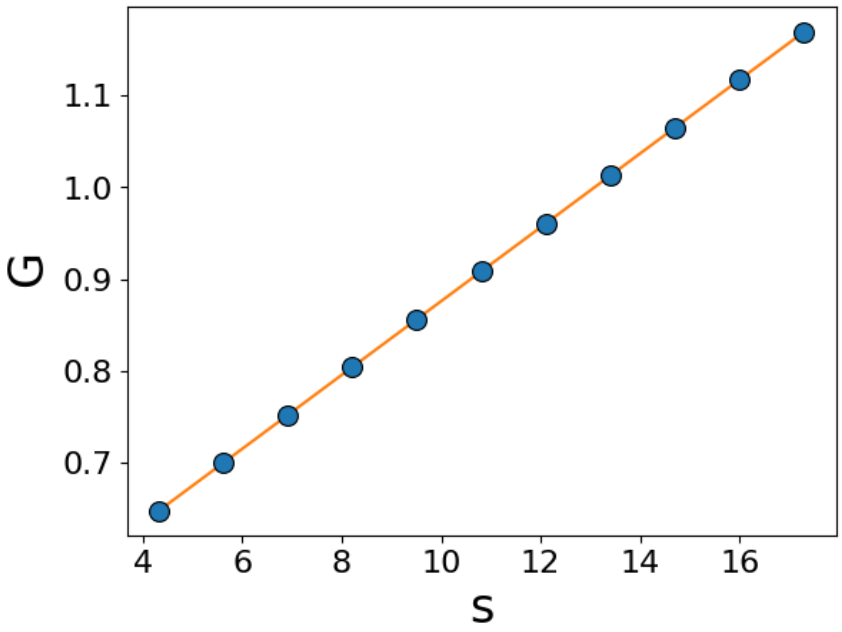

Figure 2.5: A plot of G as a function of the pump saturation parameter s predicted by Eq. (2.34). The range of s is estimated from the test pump powers and the estimated pump saturation power $P_{\mathrm{sat}} = 1.994$ mW. G is composed by applying the standard values of Δ, P_{r} and the estimated values of P_{sat}, $P_{\mathrm{r,sat}}$ to Eq. (2.34). The solid straight line indicates that G can be discussed as a linear function of s in this situation.

When the test pump laser detuning Δ and the test repump laser power P_r are fixed, Eq. (2.35) indicates a linear relationship between G and P, with the slope

$$m_G^{(4)} = \frac{1}{\xi_{std}^{(4)}} \frac{1}{P_{sat}} \left(1 + \epsilon(k_r - 3)\frac{A}{B}\right), \tag{2.36}$$

and the intercept

$$b_G^{(4)} = \left(\frac{A}{\xi_{std}^{(4)}}\right)\left(1 - 2\epsilon\frac{A}{B}\right) \approx \frac{A}{\xi_{std}^{(4)}}. \tag{2.37}$$

One can neglect the $2\epsilon A/B$ term in Eq. (2.37), considering that $2\epsilon A/B \approx 0.002 << 1$, which leads to the same form as $b_G^{(2)}$ in the two-level model. The intercept value extracted from plotting $b_G^{(4)}$ as a function of A should be zero, and the slope should be the empirical value of $1/\xi_{std}^{(4)}$. So far, a dependence of the slope $m_G^{(4)}$ on k_r shown in Eq. (2.36) is the distinction between the four-level model prediction and the two-level model. $1/\xi_{std}^{(4)}$ is a scaling factor related to the standard laser beam settings. This value may fluctuate during the measurements due to instability in the laser detunings. It is hard to compute its theoretical value because of the unknown P_{sat} and $P_{r,sat}$. Thus we can eliminate $1/\xi_{std}^{(4)}$ from the slope of G versus P using its intercept value:

$$Y = \frac{m_G^{(4)} A}{b_G^{(4)}} = \frac{1}{P_{sat}}\left[1 + \epsilon(k_r - 3)\frac{A}{B}\right]. \tag{2.38}$$

This expression shows that at a fixed repump effect ratio k_r, the normalized slope for different pump laser detunings should be linear with A/B. Extracting the slope, E, and the intercept, F, from the linear relation, the empirical value for the parameter P_{sat} is then computed as

$$P_{sat} = \frac{1}{F}, \tag{2.39}$$

and the empirical repump saturation power $P_{r,sat}$ is

$$P_{r,sat} = P_r(k_r - 2) = P_r\left(\frac{E}{\epsilon F} + 1\right). \tag{2.40}$$

Dealing With Errors in the Laser Detuning

It is important to use the true pump laser frequency detuning values in the calculation since it is related to the values of Y, E, and F. However, the pump frequency may shift over the duration of the experiment, due to the drift in the electronics used to stabilize the laser frequency. So a pump detuning correction term Δ' is added to Δ to define the true detuning value: $\Delta_t = \Delta + \Delta'$. To determine this correction, the

intercept of G versus P for different pump laser detunings, b_{G}, can be expressed as a function of Δ':

$$b_{\mathrm{G}}^{(4)} = \frac{A}{\xi_{\mathrm{std}}^{(4)}} = \frac{1}{\xi_{\mathrm{std}}^{(4)}} \left[1 + \left(\frac{2(\Delta + \Delta')}{\gamma} \right)^2 \right]. \tag{2.41}$$

$\xi_{\mathrm{std}}^{(4)}$ has a complicated expression, its definition is

$$\xi_{\mathrm{std}}^{(4)} = (A_{\mathrm{std}} + s_{\mathrm{std}}) \frac{W_{\mathrm{std}}}{H_{\mathrm{std}}}, \tag{2.42}$$

where the terms $H_{\mathrm{std}} = [B_{\mathrm{std}} + 2\epsilon(A_{\mathrm{std}} + s_{\mathrm{std}})]/(B_{\mathrm{std}} + \epsilon s_{\mathrm{std}})$, and $W_{\mathrm{std}} = 1 + k_{\mathrm{r,std}} \epsilon s_{\mathrm{std}} (A_{\mathrm{std}} + s_{\mathrm{std}}/2)/[(B_{\mathrm{std}} + \epsilon s_{\mathrm{std}})(A_{\mathrm{std}} + s_{\mathrm{std}})]$. Concerning the relative sizes of the parameters used in the equation as mentioned before, one can obtain the result that $H_{\mathrm{std}}/W_{\mathrm{std}} \approx 1$. Thus $\xi_{\mathrm{std}}^{(4)}$ can be expressed by the simple form:

$$\begin{aligned} \xi_{\mathrm{std}}^{(4)} &\approx A_{\mathrm{std}} + s_{\mathrm{std}} \\ &= \frac{4(\Delta_{\mathrm{std}} + \Delta')^2}{\gamma^2} + s_{\mathrm{std}} + 1. \end{aligned} \tag{2.43}$$

Eq. (2.43) has the same function as the two-level common scaling factor $\xi_{\mathrm{std}}^{(2)}$. This is not surprising, since in the case of a two-level model $H \to 1$ and $W \to 1$.

The intercept value of G versus P is redefined by combining Eq. (2.41) and Eq. (2.43),

$$b_{\mathrm{G}}^{(4)} = \frac{4(\Delta + \Delta')^2 + \gamma^2}{4(\Delta_{\mathrm{std}} + \Delta')^2 + \gamma^2 (s_{\mathrm{std}} + 1)}. \tag{2.44}$$

It is noted that the simplified equations Eq. (2.43) and Eq. (2.44) have no dependence on k_{r}, and are only related to the pump laser. The intercept values $b_{\mathrm{G}}^{(4)}$ is fitted as a function of the original pump frequency detunings Δ referring to this equation, while the detuning correction Δ' and the standard pump saturation parameter s_{sat} are treated as constant values. The actual detuning values are then calculated and used in the equations (2.38), (2.39), (2.40).

On the other hand, the repump laser frequency may also shift during the experiment. This leads to a new definition of k_{r}' with a parameter A_{r} added in the equation:

$$k_{\mathrm{r}}' = 2 + A_{\mathrm{r}} \frac{P_{\mathrm{r,sat}}}{P_{\mathrm{r}}}. \tag{2.45}$$

Here

$$A_{\mathrm{r}} = 1 + \left(\frac{2\Delta_{\mathrm{r}}}{\gamma} \right)^2, \tag{2.46}$$

where Δ_r is the detuning of the repump laser frequency from the repump transition $F = 1 \rightarrow F = 2'$. If the repump light gives a resonant excitation, Δ_r goes to zero, k_r' has the same form as k_r in Eq. (2.27). As a result, we can only compute the value of the repump saturation power $P_{r,sat}$ multiplied by the repump detuning-dependent parameter A_r, since the value of A_r is hard to estimate from the measurement.

2.3 Excited-State Fraction

In many experiments involving magneto-optical traps, it is imperative to know the fraction of atoms left in an excited state by the cooling and trapping lasers. In our work, we specifically would like to know the excited state fraction to allow us to measure the loss rate of the background atoms due to collisions with the trapped ^{87}Rb atoms in ground state and in excited state, which can help using the MOT as an atomic primary pressure standard. In the four-level atom model, the excited-state fraction of the atoms in the MOT can be determined from the ratio of atom numbers: $f_e^{(4)} = (n_3 + n_4)/N$. Eq. (2.21) and Eq. (2.24) are combined to get the complete form of $f_e^{(4)}$ as

$$\begin{aligned} f_e^{(4)} &= \frac{n_3 + n_4}{N} \\ &= \frac{1}{D}\left(\frac{2\Gamma_{23}/\gamma}{1 + 2\Gamma_{23}/\gamma} + \frac{\Gamma_{24}/\gamma}{1 + \Gamma_{24}/\gamma}\right) \\ &= \left[\frac{s}{2(A+s)}\right]\left(\frac{H}{W}\right), \end{aligned} \tag{2.47}$$

where H and W are defined in Eq. (2.26). Recall that $G_4 = (1/\xi_{std}^{(4)})(A+s)(W/H)$ in Eq. (2.28), one can thus express $f_e^{(4)}$ as a function of G_4 and use the simplified form of G_4 in Eq. (2.35) to interpret $f_e^{(4)}$. The obtained function is

$$f_e^{(4)} = \frac{s}{2\xi_{std}^{(4)} G_4}. \tag{2.48}$$

Using the simplified equation of G_4 in Eq. (2.35), the excited-state fraction can be approximated as

$$f_e^{(4)} \approx \frac{s}{2\left[A\left(1 - 2\epsilon\frac{A}{B}\right) + s\left(1 + \epsilon(k_r - 3)\frac{A}{B}\right)\right]}, \tag{2.49}$$

recalling that $s = I/I_{sat} = P/P_{sat}$, and A, B are detuning-dependent parameters. This equation provides a method to determine the excited-state fraction by measuring the the powers and detunings of the pump and repump lasers, and it hinges on being able to properly measure P_{sat} and $P_{r,sat}$.

For comparison, in the two-level model B goes to infinity, the function of $f_e^{(2)}$ gets more simple as

$$f_e^{(2)} = \frac{s}{2(A+s)}, \tag{2.50}$$

which only depends on the pump saturation parameter s, and the detuning of the pump laser.

2.4 Atomic Model Contrast

In section 2.2, a two-level model and a four-level atomic model are introduced to describe the atomic transitions of the ^{87}Rb atoms. The derived equations of the experimental parameter G in Eq. (2.16) and Eq. (2.35) both indicates a linear relationship between G and the pump power P, with the extracted intercept $b_G = A/\xi_{std}$. In particular, the four-level model which takes the repump transition into account has a dependence on the repump effect ratio k_r in the slope of G as $m_G^{(4)} = (1 + \epsilon(k_r - 3)A/B)/(\xi_{std}^{(4)} P_{sat})$, while in the two-level model $m_G^{(2)} = 1/(\xi_{std}^{(2)} P_{sat})$ is a constant. This results to a dependence on k_r in the excited-state fraction of the trapped atoms as well.

Fig. 2.6 predicts the behavior of f_e in the two-level model (Eq. 2.50) and the four-level model (Eq. 2.49), as a function of the repump saturation parameter $s_r = I_r/I_{r,sat}$. The standard pump laser setting is used in the calculation. The two-level excited fraction is a constant in the figure since it is not related to the repump transition. By contrast, the four-level excited-state fraction has more dependence on the low s_r, and goes to be equal to the two-level value as s_r increases. It is important to note that this increase in $f_e^{(4)}$ corresponds to a repump saturation parameter smaller than 0.1, and may be negligible for large s_r.

For comparison, Fig. 2.7 shows that the excited-state fraction in the two different models tends to have different limiting values when s goes to infinity, with a small value of $s_r = 0.003$. For $f_e^{(2)} = s/2(A+s)$, the excited-state fraction approaches to 0.5 as s is much greater than A, while the limit of $f_e^{(4)}$ is lower than 0.5 due to the repump term $\epsilon(k_r - 3)A/B$ in Eq. (2.49). The inset figure in Fig. 2.7 illustrates the behavior of f_e in the range of the s value I can obtain, showing that $f_e^{(4)}$ is 15% lower than $f_e^{(2)}$ for s = 30.

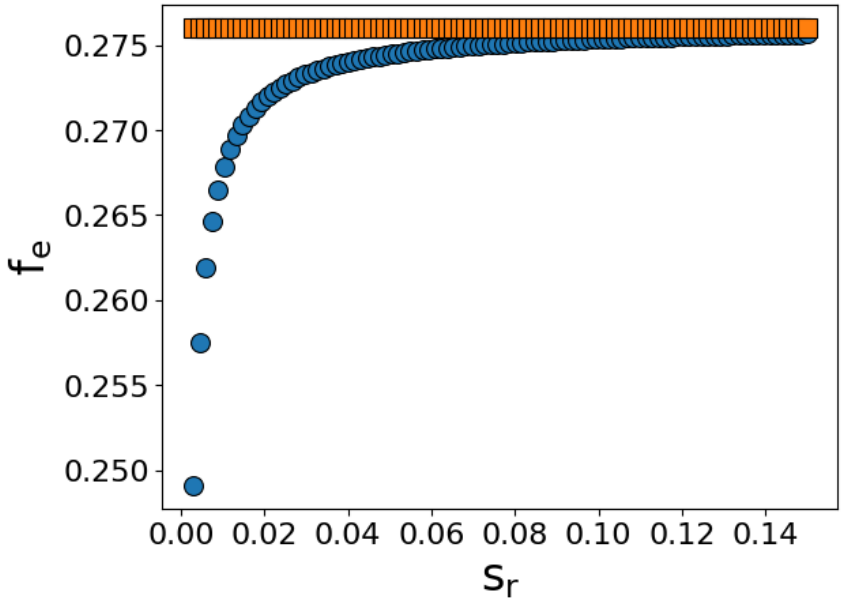

Figure 2.6: Predictions of the atomic excited-state fraction in the two-level model (■) and the four-level model (●) for different repump saturation parameter $s_r = I_r/I_{r,sat}$. The calculation is based on the standard pump laser settings, P_{std} = 18 mW and Δ = -10 MHz. A dependence of $f_e^{(4)}$ on s_r is shown in the figure, while $f_e^{(2)}$ is a constant.

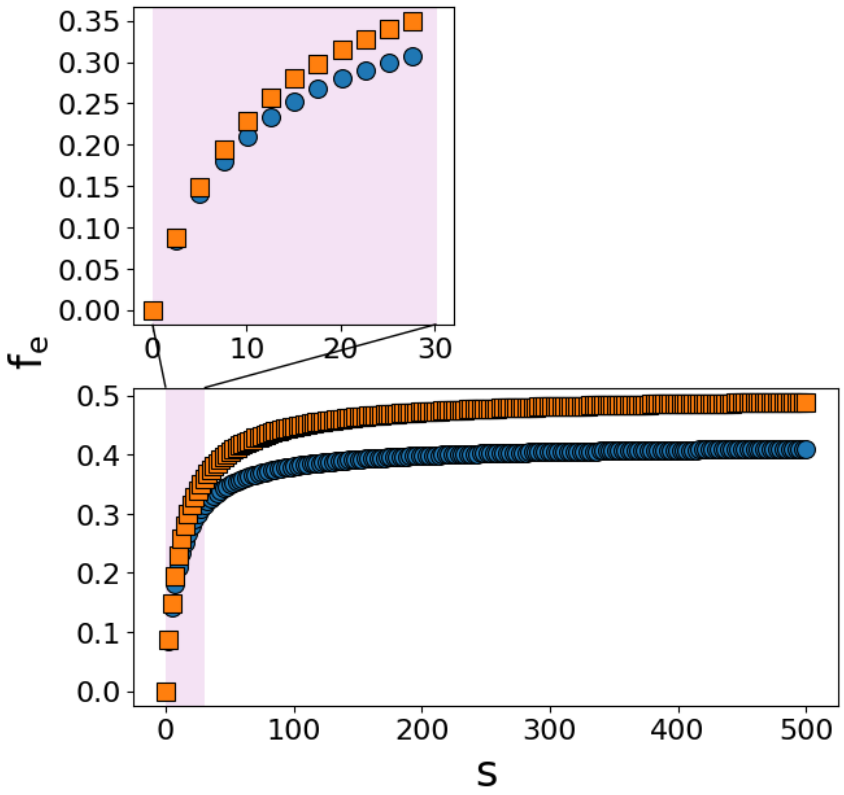

Figure 2.7: Predictions of the atomic excited-state fraction in the two-level model (■) and the four-level model (●) for different pump saturation parameter $s = I/I_{\mathrm{sat}}$. In this estimation $s_{\mathrm{r}} = 0.003$, Δ = -10 MHz. $f_{\mathrm{e}}^{(2)}$ is higher than $f_{\mathrm{e}}^{(4)}$ in this situation, and these two quantities go to different limiting values when s goes to infinity.

Chapter 3

Apparatus and Procedure of Measurements

This chapter contains two sections: the experimental apparatus and the experimental procedures. The apparatus section describes the FPGA controller, the optical setup which produces the pump and repump light to the MOT table, and the MOT chamber and its surrounding components arranged to trap atoms. In the experimental procedure, the preparation of the optics and electronic devices and the method of measuring and fitting the fluorescence from the MOT are introduced.

3.1 Experimental Apparatus

The MOT apparatus is composed of three systems: the optical setup which produces and delivers the laser light, the MOT vacuum arranged to generate a trap, and the FPGA controller connected to a computer used to control the laser frequencies, intensities, magnetic field, and event sequence timing. The first two parts of the experimental apparatus are described in details in sections 3.1.2 and 3.1.3, respectively.

Fig. 3.1 shows an overview of the apparatus and the command and control relationship between the devices. The optical setup amplifies narrow linewidth light from the master table, and controls the laser intensities as well as detunings by acousto-optic modulators (AOMs) from IntraAction (model ATD-801A2 for pump laser, model ATM-901A2 for repump laser). The direct digital synthesizers (DDS) generate the RF signals that are used to drive the AOMs. A shutter for each laser controls the access of the light to the AOM. The pump and repump laser beams, each with a specific intensity and a frequency, then get combined in beam splitters and are sent to the MOT in three dimensions. Next, a magneto-optical trap of rubidium atoms is generated with a magnetic field produced by a pair of anti-Helmholtz coils. The background rubidium vapour is released from the rubidium dispenser.

The system is controlled using custom built python scripts which translate the instructions into time-ordered sequences of events run by the FPGA (Terasic, model DE1-SoC). the timing of the sequency for each experimental run is accurate to

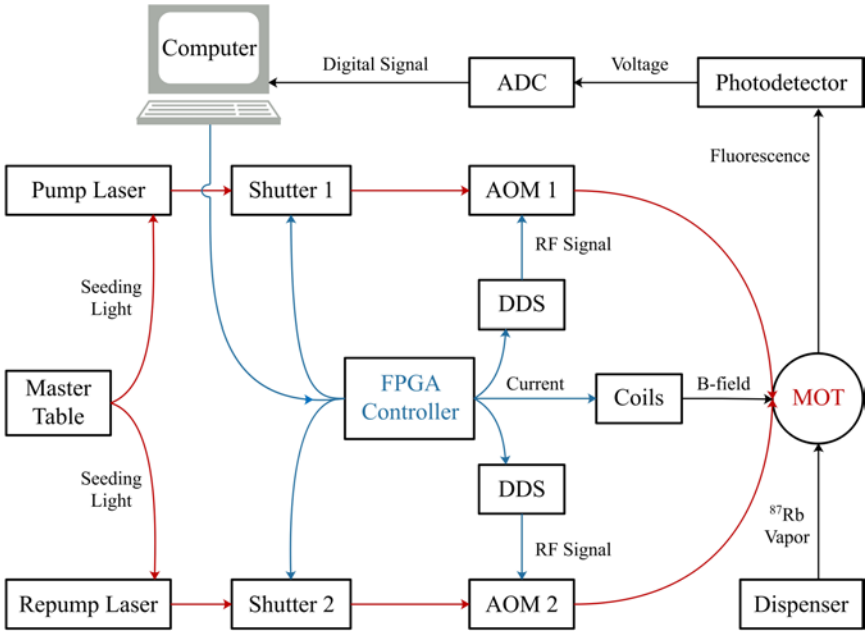

Figure 3.1: Block diagram of an overview of the experimental apparatus. To generate a magneto-optical trap, narrow linewidth pump and repump light from the master table is injected into separate slave laser amplifiers. The slave laser output beams' intensities and frequencies are controlled by AOMs. A computer talks to the FPGA controller which sets the input signal of the DDS, the current in the magnetic field coils, and the opening/closing of two mechanical shutters. The DDS generates the RF signals that are used to drive the AOMs. Rubidium atoms released from the dispenser thus get trapped in the overlapping region of the laser beams and the emitted fluorescence is measured from a photodetector connected to the computer via an ADC.

within 1 μs. The AOM settings, the driving current of the magnetic coils, and the mechanical shutters are preset in the python scripts and managed by the FPGA controller as well. A photodetector collects the fluorescence from the MOT and sends the voltage signal to the computer through an analog to digital converter (ADC).

3.1.1 Optical Setup

The optical setup of the experiment is illustrated in Fig. 3.2. The seeding pump and repump laser light with narrow linewidth is generated on a separate master table where it is then sent through fibers to the optical table for the experiment. The light is then coupled to the slave laser through an isolator and get amplified to around 60 mW. The laser diodes used in the slaves are from Thorlab, part number L785P090. A mechanical shutter controls the access of the light to an optical beam splitter, where a small reflection of the light is coupled into a fiber as a diagnostic signal to check the injection of the master light on an oscilloscope. The rest of the light is transmitted through the beam splitter into a double-pass AOM setup.

In the double-pass AOM setup, the intensity and frequency of the light can be changed to certain values, which is achieved by an acousto-optic modulator (AOM), and the polarization direction of the light is shifted by a quarter waveplate. Light from the beam splitter passes through the AOM, after which the first-order diffracted light deviates from the zeroth-order light with an angle. A plano-convex lens of focal length f = 150 mm placed after the AOM ensures that the passed first-order diffracted light is parallel to the zeroth order. The zeroth order beam is blocked while the first order gets reflected back from a planar mirror in the original path. From these two passes through the AOM, the output frequency is increased by twice the AOM frequency. Since the light from the master table is detuned 180MHz below the pump or repump transition, the RF frequency driving the AOM, ν_{AOM}, should be set as

$$\nu_{\mathrm{AOM}} = \frac{180 + \Delta}{2}, \tag{3.1}$$

where Δ is the desired detuning of the laser. The intensity of the light depends on the amplitude of the RF driving signal sent to the AOM, and the RF signals are generated by direct digital synthesizers (DDS) and amplified before going to the AOMs. The amplitude and frequency of the RF signal operating the AOM, as well as the status of the mechanical shutter, are set via the FPGA controller. Moreover, a quarter waveplate placed between the convex lens and the planar mirror shifts the polarization direction of the light as it double passes the waveplate, and blocks the zeroth-order diffracted light. Therefore, the diffracted beam returned through the AOM is now reflected from the polarizing beam splitter and gets magnified by two lenses. The total power of the laser is measured behind the concave lens, which

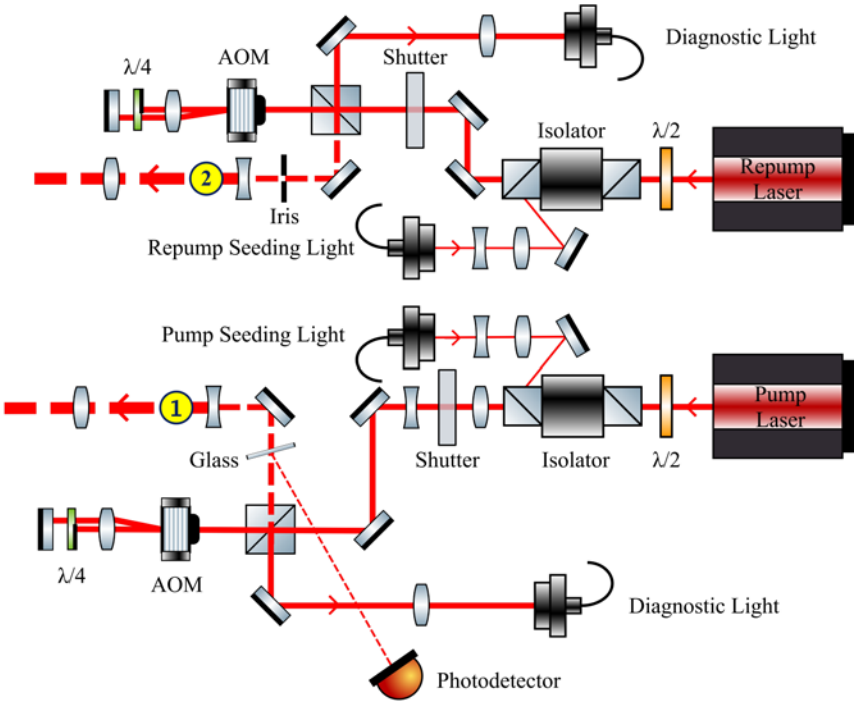

Figure 3.2: A schematic diagram of the pump and repump laser amplification setups [**?**]. Each slave laser is seeded by a narrow linewidth light from the master table through an isolator. The laser beam then gets through the shutter and is split by a beam splitter, the reflection from which is coupled into a fiber as a diagnostic light to check the injection. Next, the transmitted light is sent to a double-pass AOM setup, where the intensity of the first-order diffracted light is controlled by setting the AOM amplitude, and its frequency is increased by twice the AOM frequency. A quarter waveplate shifts the polarization direction of the light as it double passes the waveplate, and blocks the zeroth-order diffracted light. Consequently, the beam returned through the AOM is reflected from the beam splitter and gets magnified by two lenses. The combination of these two beams with specific frequencies and intensities is sent to the MOT to trap atoms. The total powers in the pump and repump beams before entering the MOT devices were measured by a power meter, whose sensor is conveniently placed at positions ① (pump) and ② (repump) in the figure.

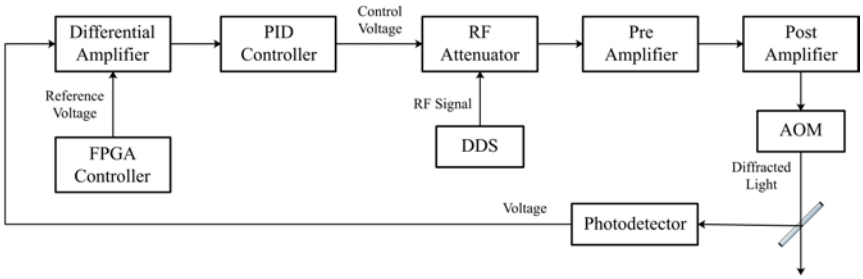

Figure 3.3: Block diagram of the intensity stabilization system of the pump laser. The feedback in the loop is from a small reflection of the pump laser detected by a photodetector. The PID controller reads the error signal from the differential amplifier and accordingly outputs a control voltage to the RF attenuator, which controls the RF signal from the DDS and thus pushes the laser intensity towards stability.

is a convenient location to place the sensor of the power meter (Coherent, model LabMax T0).

The intensity of the pump laser light is stabilized using a feedback loop consisting of a photodetector, a differential amplifier, a proportional-integral derivative (PID) controller, and a RF attenuator (see Fig. 3.3). The pump beam after the double-pass AOM arrangement is reflected by a piece of glass and sent to a photodetector. The output voltage of the photodetector, as well as the preset reference voltage from the FPGA controller, are compared in the differential amplifier, providing an error signal to the PID controller. The PID controller then applies a correction to its control function according to the input signal and controls the RF driving signal by a RF attenuator. Therefore, the controller continuously reads the feedback and corrects the control function, until the detected light voltage is equal to the reference voltage so the laser intensity is stabilized.

3.1.2 MOT Chamber

To generate a magneto-optical trap, a MOT system was set up, which consists of a rubidium vacuum cell, MOT laser beams, magnetic coils, and a photodetector (see Fig. 3.4). The output light of the pump and repump lasers from the optical setup in Fig. 3.2 is combined and sent to the MOT table in three dimensions, where the pump beam is evenly distributed in all three perpendicular directions with the powers of $P_{\mathrm{x}} = 3.72$, $P_{\mathrm{y}} = 3.50$, $P_{\mathrm{z}} = 3.26$ mW. The repump beam is only sent along the two horizontal directions with the powers of $P_{\mathrm{r,x}} = 2.60$ and $P_{\mathrm{r,y}} = 2.90$ mW. The combination and the power distribution of the light are accomplished by using optical beam splitters and half waveplates. After that, the linearly polarized beam passes through a quarter waveplate, which converts the light into circularly polarized light. The light in each arm is then transmitted through the glass cell, and passes through a second quarter waveplate located in front of a retro-reflection mirror, completing each beam arm. From this configuration, the retroreflected light has the same circular polarization as the incoming beam, thus completes a pair of counter-propagating laser beam. Consequently, three orthogonal counter-propagating pairs of laser beams along three orthogonal spatial axes get crossed at the 1 cm length vapor cell, trapping atoms with the help of a magnetic field produced by the coils, as shown in Fig. 3.4 (a).

The background rubidium vapor is released by energizing the rubidium dispenser. It is typically loaded for 3 min at a current of 5.3 A, around once a week. After energizing the dispenser, the rubidium vapor density decreases for one day before coming to equilibrium when the test data can be acquired. An optical collection system consisting of a convex lens of focal length f = 35 mm set towards the vacuum cell, an optical iris, and a photodetector, collects the fluorescence through

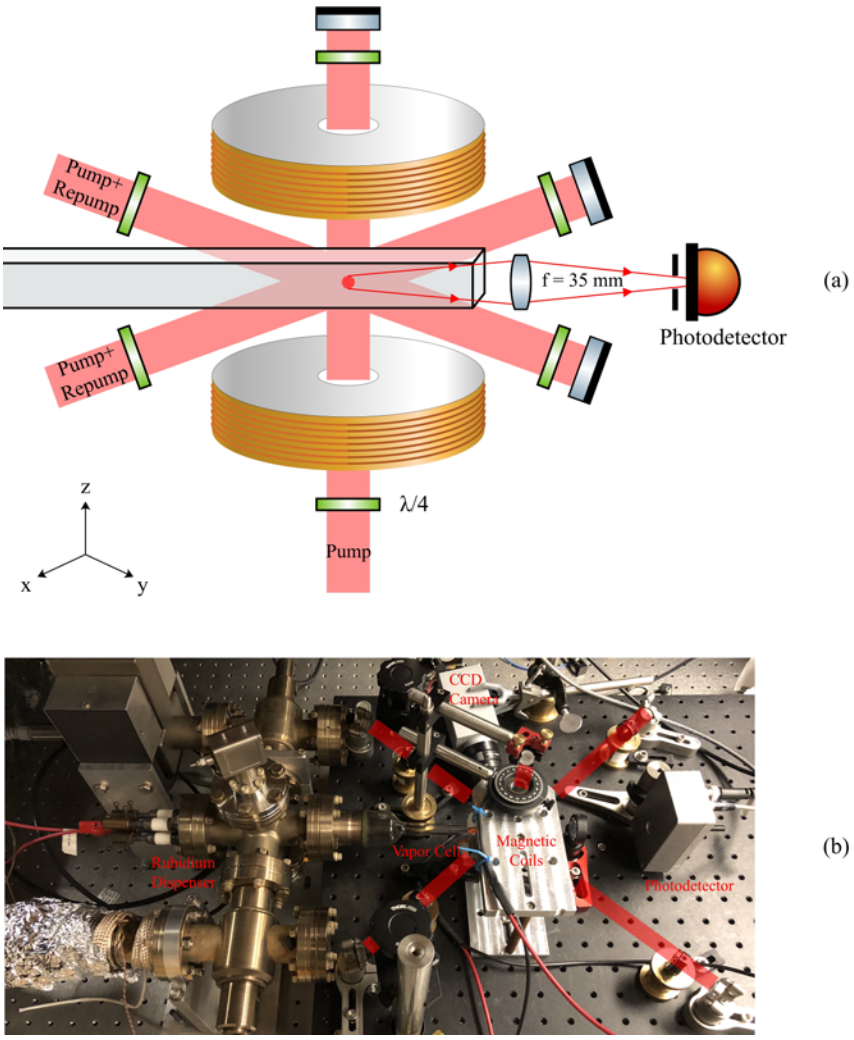

Figure 3.4: Diagrams of the MOT setups. (a) is a schematic of the MOT system which contains a vapor cell, MOT laser beams, mirrors, quarter waveplates, magnetic coils, and a photodetector. The laser light shown as red lines is sent from the optical setups in Fig. 3.2 and crossed in the cell. The two laser beams in x and y directions are mixture of the pump and repump light, while the vertical beam is coming from the pump light. Two quarter waveplates and a mirror for each optical path enable the same circular polarization for the incoming and retroreflected beams. An optical collection system collects the fluorescence through the end window of the vacuum cell. An overview of the MOT system can be seen in a picture (b).

the end window of the vacuum cell. This system collects over a solid angle of 0.071 sr and passes through an aperture of 6 mm to limit the scattered light transmitted to the photodiode. A CCD camera is used to observe the status of the MOT in the cell. A picture of the MOT system is displayed in Fig. 3.4 (b).

3.2 Experimental Procedure

In the experimental procedure, the background scattered light for different laser settings are firstly recorded, then the atoms in the cell are loaded into a MOT, and the fluorescence due to the trapped atoms under different laser frequency and amplitude is measured. Care was taken to insure the reproducibility and accuracy of the measurements. Section 3.2.1 tells the determination of the useful repump power range, and section 3.2.2 introduces the calibration of the photodetector. The details of the measuring steps, as well as the recording of the fluorescence, are shown in section 3.3.3.

3.2.1 Repump Saturation Determination

The goal of the experiments is to verify the predictions of the four-level atomic model. In particular, we want to extract the empirical parameters, P_{sat}, $P_{\mathrm{r,sat}}$, and use these to estimate the fraction of atoms in electronic states as a function of the MOT trap parameters. Pump transition plays a lead role in the cycling transition of atoms, while repump light is used to pump the atoms in the F = 1 ground state back into the cycling transition, which is an occasion with small possibility. Therefore, recognizing the useful range of the repump laser power is essential in the experiment. Before the measurement of G parameter, the fluorescence voltage due to the steady-state MOT is plotted as a function of different repump powers. For these measurements the pump laser parameters were fixed at P = 18 mW, Δ = -10 MHz, Δ_{r} = 0 MHz, and B-field current = 0.5 A (field gradient to 12 G/cm). The results are given in Fig. 3.5. The steady-state MOT voltage increases rapidly when the repump power increases roughly from 0.2 mW to 0.5 mW, then it slows down and gets saturated as the repump power is greater than 0.8 mW. This implies that only $P_{\mathrm{r}} \approx 0.5$ mW is required for the repump light to saturate the cycling of atoms in the dark state in the MOT. Consequently, the repump laser power is set lower than 0.5 mW in the next experiment to observe the atom's dependence on the repump power.

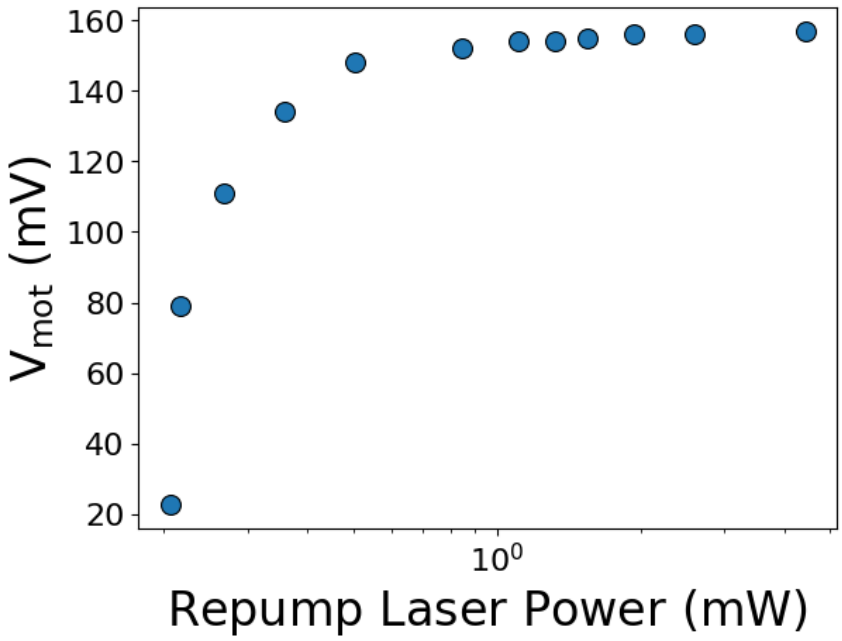

Figure 3.5: A plot of the voltage of steady-state MOT versus the repump laser power. The fluorescence voltage of the steady-state MOT stops its rapid growth after the repump power reaches 0.5 mW; therefore the repump power should be lower than 0.5 mW in the next experiment.

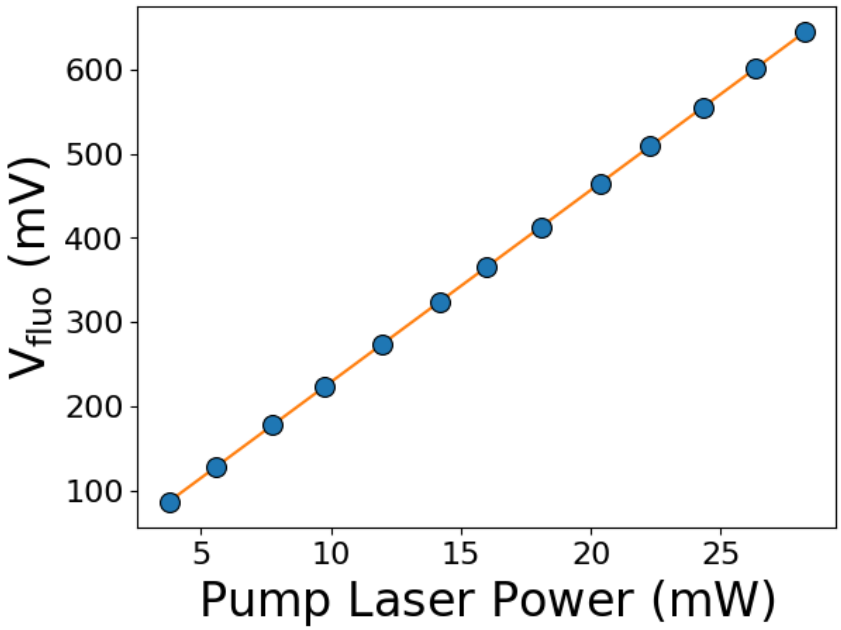

Figure 3.6: A plot of the voltage of the scattered light signal due to the pump laser versus the corresponding pump power when Δ = -10 MHz. There is a linear relationship between the scattered light signal voltage V_{pump} and the power P. A simple equation V_{fluo} = (22.80 (0.09) P) mV is fitted to show the association.

3.2.2 Photodetector Calibration

The voltage signal due to the trapped atoms, V, is equal to the fluorescence of the steady-state MOT, $V_{\text{ss,mot}}$, minus the baseline signal of the scattered light from the lasers, $V_{\text{ss,zero}}$:

$$V = V_{\text{ss,mot}} - V_{\text{ss,zero}} \tag{3.2}$$

for each setting. Accordingly, the voltage of the pump laser power is computed by subtracting the background light V_{off} from the pump laser scattering into the photodiode $V_{\text{pump on}}$:

$$V_{\text{pump}} = V_{\text{pump on}} - V_{\text{off}}. \tag{3.3}$$

The fluorescence from the MOT, which is our primary measurement quantity in the MOT experiment, is collected by focusing the light on a photodetector with a 1 cm × 1 cm sensor. Thus it is crucial to make sure that the reading of the photodetector is correct and reasonable. To test and calibrate the photodetector, the total power in the pump beam before entering the vapor cell was measured by a calibrated power meter as a function of the AOM amplitude setting, and compared to the photodetector readings. The power meter was placed at a location before the laser beams are split and sent to the MOT table, labelled in Fig. 3.2.

Meanwhile, the voltages generated by pump light scattering corresponding to the measured pump powers were recorded in the computer. The background light was subtracted from the pump laser scattering into the photodiode according to Eq. (3.3). We expect that the collected fluorescence of the pump laser is linearly related to the pump power measured by the power meter, and Fig. 3.6 verifies this prediction with a negligible intercept. Hence it is adequate to use the photodiode voltages $V_{\text{pump}}^{\text{test}}/V_{\text{pump}}^{\text{std}}$ instead of measuring the actual optical powers P/P_{std} to determine the empirical parameter G (once the calibration of P to V is known). The measured scattered light signal voltage V_{pump} can be converted to powers P as well when concerning the relationship between G and P in Eq. (2.35).

3.2.3 Fluorescence Measurement

From Eq. (2.34), one can conclude that the saturation power parameter, P_{sat}, is quantified by setting arbitrary laser parameters and loading the MOT to equilibrium, then quickly switching the settings to a test set of values to read. In the preparation of the measurement, the slave lasers were well injected, and the master lasers were locked at the correct frequencies. The double-pass AOMs were well aligned so that the laser beams on the MOT table would not move when changing the laser detunings from -30 MHz to 30 MHz. Particular attention was paid when aligning the laser beams to generate a MOT under various laser settings. The spatial

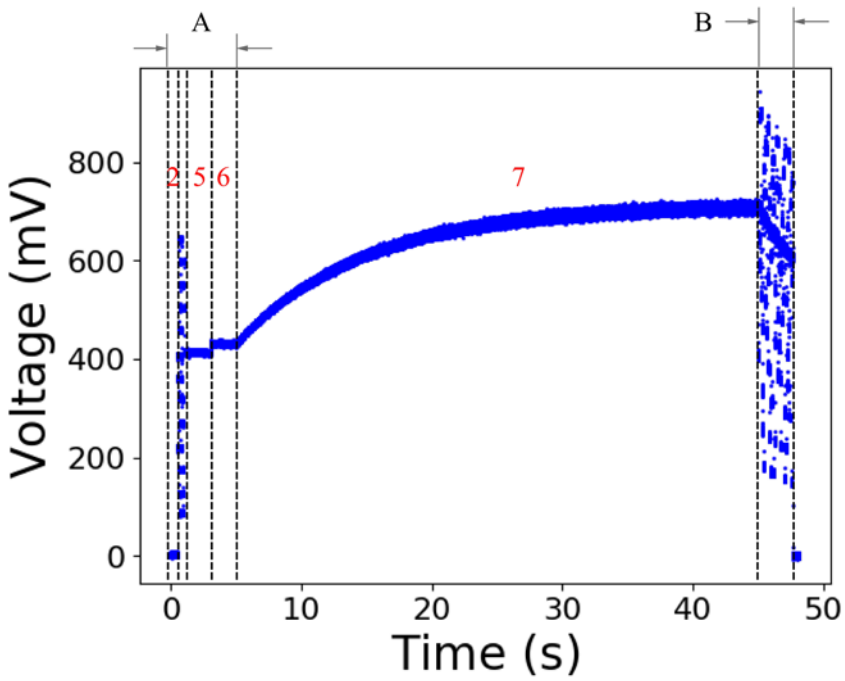

Figure 3.7: A plot of the voltage signal collected from the photodetector versus time. In this figure, Δ = -8 MHz, P_r = 0.009 mW, and the pump test power P was varied from 7 mW to 28 mW. Section A and section B labelled in the figure represent the background scattered light and the fluorescence signal due to the trapped atoms, respectively. In section A, step 2 is the signal of the background light while the lasers and magnetic field were all off, step 5 shows the scattered light of the pump laser at the standard settings. In step 6 pump and repump lasers were all turned on under the standard settings, then the magnetic field was turned on at 0.5 A to trap atoms in step 7. Measurements made in a short amount of time, which are in the sections A and B in the figure, are plotted in Fig. 3.8 and Fig. 3.9 respectively for more unobstructed view.

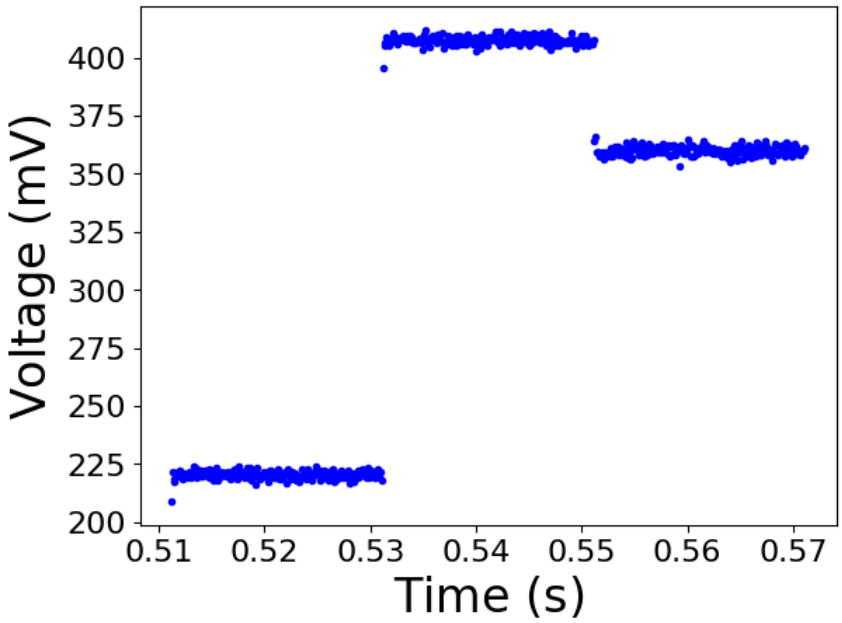

Figure 3.8: A plot of the details of section A in Fig. 3.7. The three signal levels are different voltages of the pump scattered light with different pump powers when the pump detuning was set to -8 MHz.

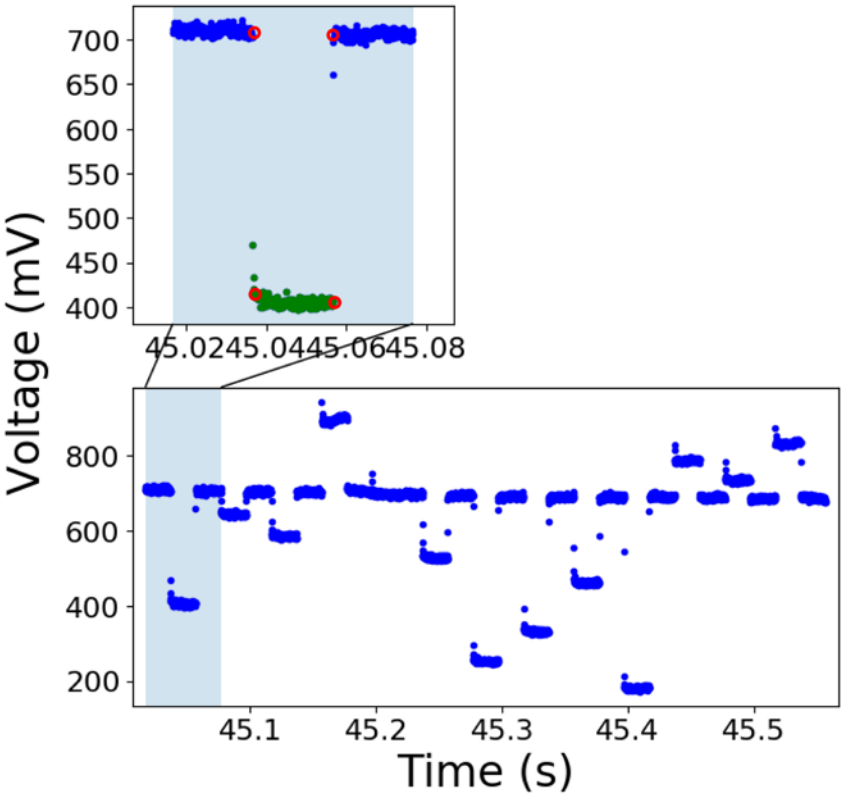

Figure 3.9: A plot of the details of section B in Fig. 3.7. The main figure displays the fluorescence voltage of the MOT when the power and detuning of the pump laser, as well as the repump power, were switched back and forth between 13 different "test" values and 1 set of "standard" values, the procedure of which is described in step 8 in the measurement method. The inset figure above the main plot shows a specific fluorescence change from the MOT when the laser settings were turned from "standard" (P_{std} = 18 mW, Δ_{std} = -10 MHz, $P_{\mathrm{r,std}}$ = 0.483 mW, labelled by blue color) to "test" (P = 13 mW, Δ = -8 MHz, P_{r} = 0.009 mW, labelled by green color), then back to "standard" (blue). During this period, the fluorescent voltage before and after the quick laser condition change generates two experimental parameters: G_{init} (switched from "standard" to "test") and G_{final} (switched from "test" to "standard"), labelled by the red circles in the inset figure. The fitting details are explained in Fig. 3.10. Moreover, one can see a decaying trend in the MOT voltage under test settings (green), which indicates an atom number loss due to the changed trapping conditions.

position shift of the MOT for different settings was minimized to avoid variations in the atom number due to changes in the laser parameters. Also, a dense MOT was avoided as it could induce multiple scattering of photons, which reduces the detected fluorescence signal from the MOT.

In our work, the procedure of a loading run to measure the empirical parameter G with a typical test repump power is listed as follows:

1. Values of Δ_{std} = -10 MHz, P_{std} = 18.0 mW, and P_{r} = 0.483 mW are selected as "standard" for these experiments. Choose a new detuning and 13 different values of power for the pump laser as "test" settings (see Table. 3.1), while the repump laser also has a new power.

2. Measure the background level V_{off} when the lasers and magnetic field are off.

3. Turn on the pump laser with test frequency and different test powers, while the repump laser is still off, and get $V^{\mathrm{test}}_{\mathrm{pump\ on}}$.

4. Turn on the lasers under various test settings to record the test baselines, $V^{\mathrm{test}}_{\mathrm{ss,zero}}$.

5. Turn off the repump laser, switch the pump laser under standard settings, and record the scattered light, $V^{\mathrm{std}}_{\mathrm{pump\ on}}$.

6. Turn on the two lasers at standard settings and measure the standard baseline $V^{\mathrm{std}}_{\mathrm{ss,zero}}$.

7. Set the driving current of the magnetic coils to 0.5 A, fill the MOT to equilibrium in 40 s, and record the fluorescence $V^{\mathrm{std}}_{\mathrm{ss,mot}}$.

8. Quickly switch the lasers to one set of test settings for 20 ms, then switch them back to the standard settings for another 20 ms. Record the fluorescent signals in the period to determine $V^{\mathrm{test}}_{\mathrm{ss,mot}}$ and $V^{\mathrm{std}}_{\mathrm{ss,mot}}$.

9. Repeat step 8 for different test powers of the pump laser.

10. Repeat step 8 and step 9 for 5 times in total, each time with random test pump powers permutations, in order to increase the accuracy of the data.

Test Pump Power (mW)												
3.79	5.60	7.77	9.78	11.96	14.19	16.00	18.10	20.36	22.29	24.31	26.32	28.22

Table 3.1: 13 different values of the pump laser power as "test" settings.

The timing of each step in the experiment and the corresponding control settings are listed in Table. 3.2. One significant advantage of this measuring method of quickly switching the laser settings back and forth between different "test" settings and one "standard" settings is that it reduces the duration of each experiment. One can notice from Table. 3.2 that it only takes 48 seconds for such a loading run, so all the measurement is expected to take less than two hours, which limits the shift in the laser power and frequency, the room temperature, and other optical and electronic devices used in the experiment, and reduces any effects related to variations in the background Rb vapour pressure.

Fig. 3.7 shows the recording of the fluorescence voltage during a typical loading run. Measurements made in a short amount of time, which are in the sections A and B in the figure, are plotted in Fig. 3.8 and Fig. 3.9 respectively. The red circles in Fig. 3.9 represents two sets of voltages $V_{\mathrm{ss,mot}}^{\mathrm{std}}$ and $V_{\mathrm{ss,mot}}^{\mathrm{test}}$, which can be used to calculate the experimental parameter G. Therefore, one G_{init} and one G_{final} are generated for each test MOT interval. We can collect 5 sets of G_{init} and 5 sets of G_{final} from Fig. 3.7 in one loading run, and the average of these 10 data sets gives a reliable final result of the parameters G.

Time (s)	0.5	0.26	0.26	2	2	40	2.6
Pump Shutter	off	on					
Pump Laser	off	on at "test"		on at "standard"			switch between "test" and "standard"
Repump Shutter	off		on	off	on		
Repump Laser	off		on at "test"	off	on at "standard"		switch between "test" and "standard"
B-field	off					on at 0.5 A	

Table 3.2: A table of the timing and control settings in the experiment. Pump and repump shutters were closed when turning off the AOMs to avoid the leakage of the zeroth-order diffracted light to the MOT.

Fluorescence Fitting

To precisely determine the value of G, the measured signal voltage was recorded in the computer and analyzed in python scripts. The voltage of the background scattered light, V_{off}, $V_{\text{pump on}}$, and $V_{\text{ss,zero}}$, were extracted by taking the averages from their corresponding light signal voltages. Fitting the MOT fluorescent voltage is more complicated since the voltage reading we need is strict with time. Fig. 3.10 shows a specific fluorescence change when the laser settings were turned from "standard" to "test". To ensure that the atom number in the MOT was the same for the "standard" and the "test" measurements, $V^{\text{test}}_{\text{ss,mot}}$ should be taken just after the switch. Therefore, the time for the experimental system to read the script instructions, change the laser settings, and record the voltage signal was determined in the first subplot in Fig. 3.10, where the scattered light voltage due to the pump laser changed from $V^{\text{std}}_{\text{pump on}}$ to $V^{\text{test}}_{\text{pump on}}$ in 300 μs (3 points). This delay labelled in the light blue region was then used in the second subplot to calculate the start point of the fluorescence due to the trapped atoms under test settings, eliminating the effect from the system delay on the fluorescence voltage change.

Based on the assumption that the fluorescence measured in the photodiode is proportional to the atom number in the trap: $\mathrm{V} \propto \mathrm{N}$, and the atom number dynamics described in Eq. (2.11), the fluorescence due to the trapped atoms, V, is fitted by an exponential model

$$V = V_0 + A(1 - e^{-\Gamma t}), \tag{3.4}$$

where V_0 is the initial voltage in the fluorescence measurement interval. A is a positive constant for a loading MOT and turns negative when the MOT is decaying. The red curve in Fig. 3.10 fits the decaying fluorescence according to this equation. Assuming that the fluorescence change during the system delayed time (300 μs) is negligible, the start point and the end point of the fitting curve were then used to obtain the best estimate of $V^{\text{test}}_{\text{ss,mot}}$, and the standard fluorescence signal $V^{\text{std}}_{\text{ss,mot}}$ was measured in the same way.

3.2.4 Atom Number Loss

Our experiment requires a fixed atom number in the MOT when changing illumination conditions from the pump and repump lasers. However, in the zoomed figure in Fig. 3.9 a decaying trend is illustrated from the MOT voltage under test settings (green points). The fluorescence from trapped atoms for a longer time is given in Fig. 3.11, where the laser settings were switched back and forth between different "test" values and one set of "standard" values. It is clearly shown that the MOT fluorescence under standard settings is decreasing in (a) from the continuous changes of the laser settings, and it roughly keeps constant in (b). The only difference in

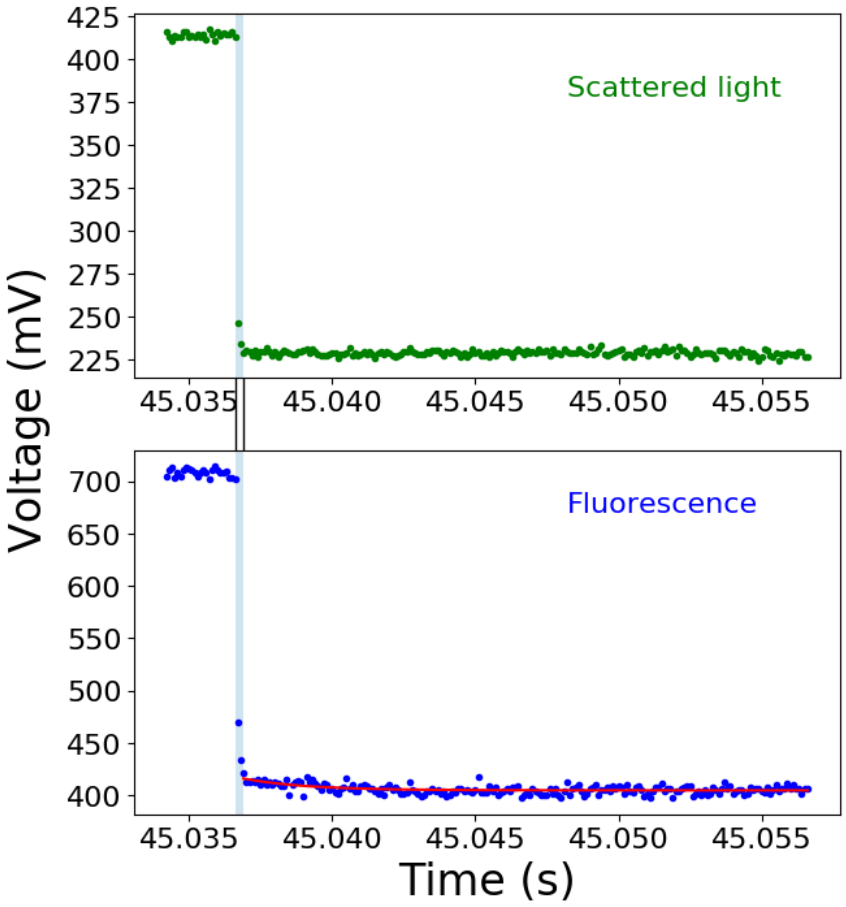

Figure 3.10: A plot of the scattered light voltage due to the pump laser and the fluorescence voltage of the MOT when the laser settings were changed from "standard" to "test". The time for the scattered light voltage to change between different settings (in the light blue region) was used in the fluorescence voltage change to determine the start point of the test fluorescence measurement interval. The interval was then fitted by a red curve according to Eq. (3.2.3) to obtain $V_{\mathrm{ss,mot}}$.

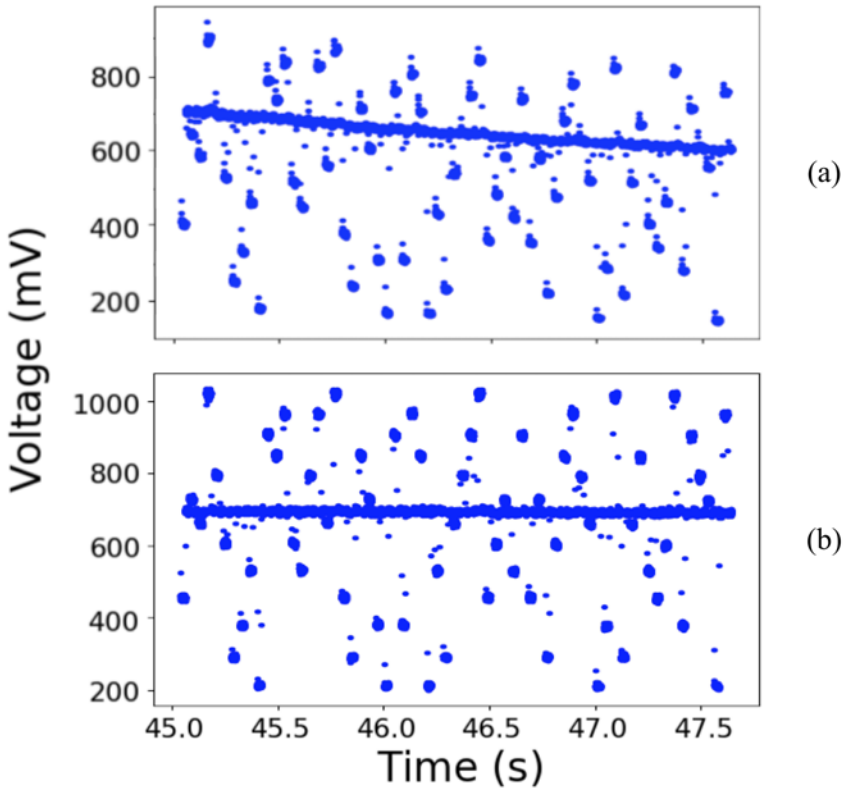

Figure 3.11: A plot of the fluorescence due to the trapped atoms under different illumination conditions. Figure (a) is an extension of Fig. 3.9, where the MOT fluorescence under standard settings is decreasing over time. In figure (b) the test repump power is changed from 0.009 mW to 0.483 mW while the standard repump power is the same as in figure (a), and the fluorescence of the standard MOT keeps constant. The comparison of these two figures points that our assumption of constant atom number is valid for the applied pump detunings, but not entirely practical for a small repump power.

the laser settings between figures (a) and (b) is the test repump power, as figure (a) has a test repump power of 0.009 mW, and in figure (b) it is equal to the standard repump power 0.483 mW. Therefore, one can say that the atom number loss during the experiment is due to the changed atom loading rate and loss rate when turning to the settings with a small repump power, which leads to a lower equilibrium atom number in that measurement interval.

To test the influence on the measurement results from this phenomenon, two data sets G_{init} and G_{final} generated from Fig. 3.9 are compared in Fig. 3.12 by calculating the ratio $(G_{\mathrm{final}} - G_{\mathrm{init}})/G_{\mathrm{init}}$. Recalling that G_{init} is measured from the fluorescence voltages of the trapped atoms when the laser settings were switched from "standard" to "test", and G_{final} is measured when switching from "test" back to "standard". If the atom number loss we observed in Fig. 3.12 is negligible in each fluorescence measurement interval, G_{init} and G_{final} should have approximately the same values. The ratio in Fig. 3.12, as we expected, fluctuates around the zero level, showing that the atom number loss during the MOT fluorescence measurement did not influence the experimental results.

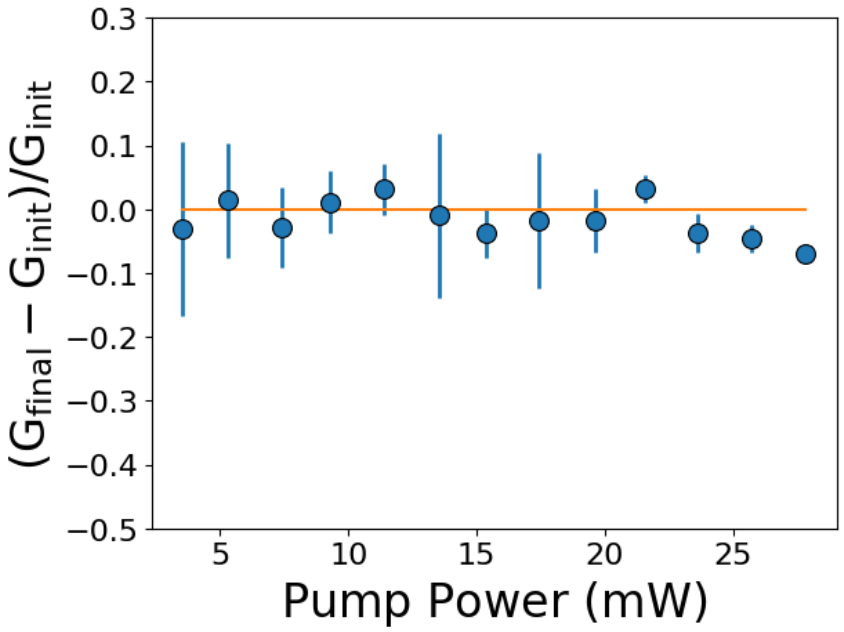

Figure 3.12: A plot of the ratio $(G_{\text{final}} - G_{\text{init}})/G_{\text{init}}$ for different test setting pump power P from Fig. 3.9. G_{init} and G_{final} were measured at the start point and the end point of the fluorescence intervals under test settings, respectively. The ratio of G fluctuates around the zero level, which is labelled by the horizontal line, showing that G_{init} and G_{final} are approximately equal and are not influenced by the atom number loss.

Chapter 4

Results

4.1 G Parameter Measurement

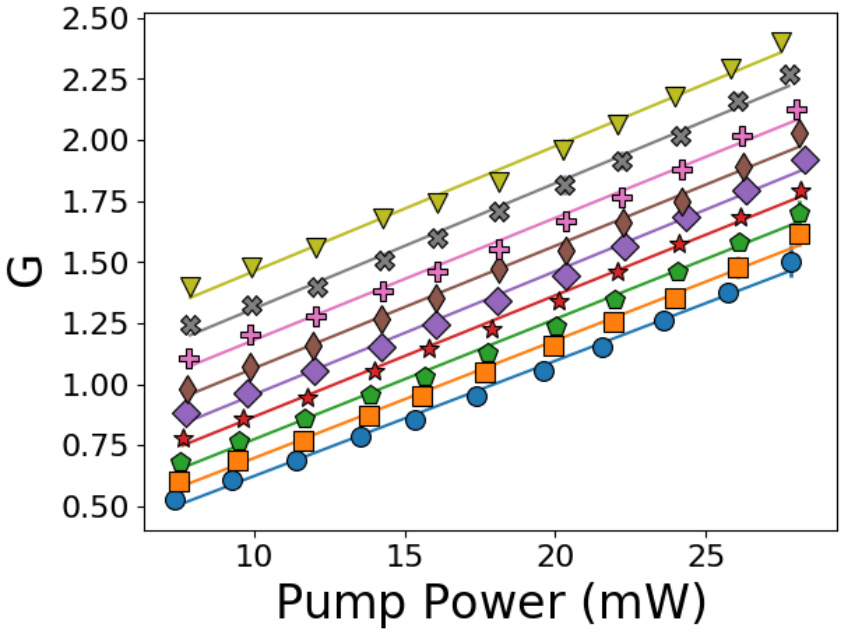

Figure 4.1: A plot of G versus the test setting pump power P. Each set of data is fitted to a line and corresponds to pump laser detunings of $\Delta/2\pi$ = -6 (●), -7 (■), -8 (⬟), -9 (★), -10 (◆), -11 (♦), -12 (✚), -13 (✖), and -14 (▼) MHz. The test repump power is held constant at 0.009 mW with no detuning.

In our work, measurements of the experimental parameter G were taken for different repump powers: 0.009, 0.011, 0.013, 0.017, 0.023, 0.029, 0.037, 0.073, and 0.483 mW, the order of which is chronological. For the repump power P_r = 0.009 mW, G is plotted as a function of the pump laser power P for each pump laser

detuning Δ in Fig. 4.1. The prediction from Eq. (2.35) and Fig. 2.5 give that G is a linear function of the test pump power, and its intercept value in Eq. (2.37) should increase with the increase of the pump detuning. The measured result shows that G values follow the predictions.

4.1.1 Determining the True Pump Detuning

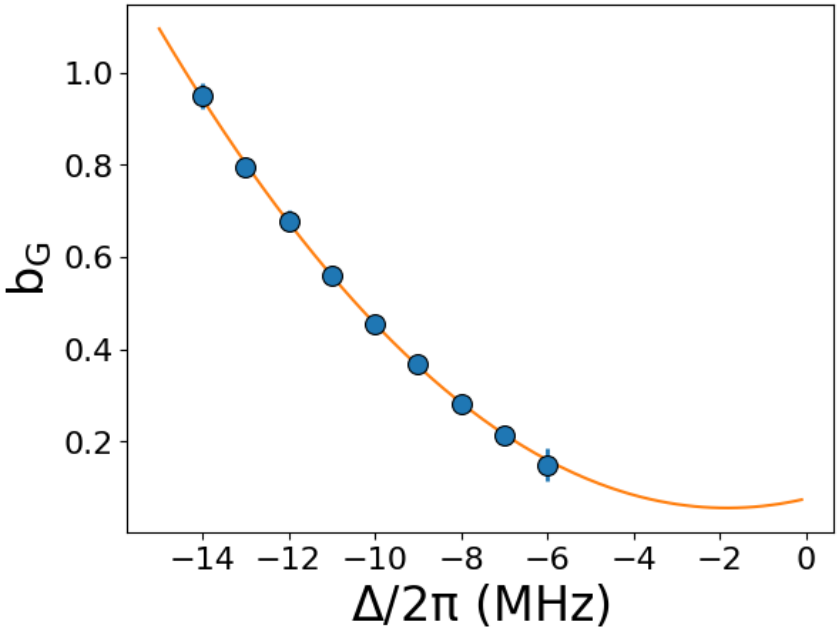

Figure 4.2: A plot of b_G as a function of the pump laser detuning Δ. The solid curve fits the intercept values using Eq. (2.44). The derived detuning correction value Δ' is utilized to modify the detuning value, and the standard saturation parameter value s_{sat} can be evidence of the accuracy of the detuning correction method, as discussed later in Fig. 4.4.

The expression of the intercept $b_G^{(4)}$ derived from Fig. 4.3 simplifies in Eq. (2.44) as $b_G = [4(\Delta+\Delta')^2+\gamma^2]/[4(\Delta_{std}+\Delta')^2+\gamma^2(s_{std}^2+1)]$, which is a function of Δ with unknown parameters Δ' and s_{std}. Therefore, the detuning error for the pump laser, Δ', can be determined by plotting the intercept $b_G^{(4)}$ as a function of the original pump laser detuning Δ, as shown in Fig. 4.2. The fitting curve according to Eq. (2.44) fits well with the intercept values, a detuning correction Δ', as well

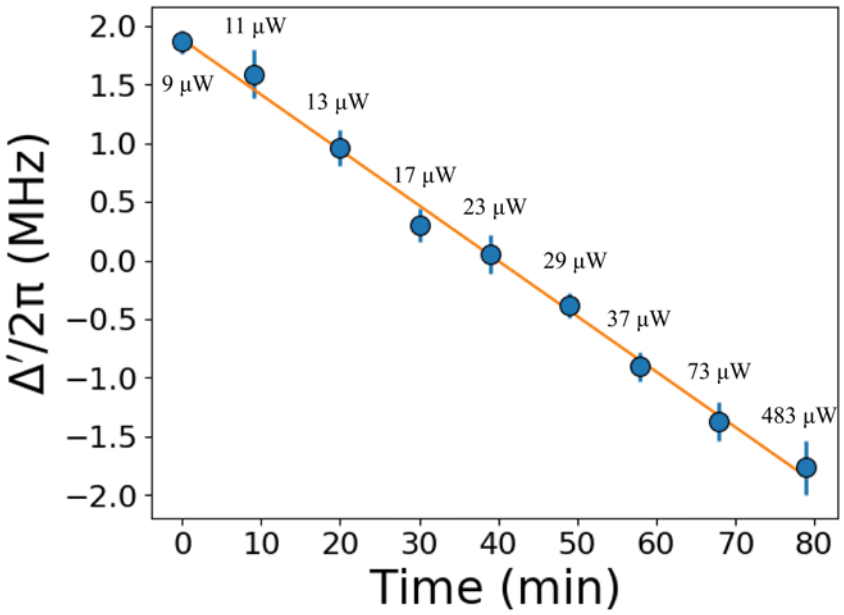

Figure 4.3: A plot of the detuning correction values Δ' for different repump powers as a function of the measured time. The test repump powers corresponding to the measured detuning corrections are labelled in the figure. The solid straight line linearly fits Δ' by the equation $\Delta'/2\pi$ = -0.0467 (0.0023) t + 1.83 (0.10) MHz, which predicts the accurate detuning value for each G versus P data set. It shows obviously that the pump laser frequency shifts linearly with time, around 3.8 MHz in 80 minutes after the laser frequency was locked to the pump transition.

as a standard pump saturation parameter s_{sat}, are hereby determined. For each test repump power, one can collect a set of b_{G} like this one, and the extracted Δ' is plotted in Fig. 4.3, in the order of the data taken time. Fig. 4.3 illustrates a linear relationship between the detuning correction value Δ' and time, which indicates that the pump laser frequency is shifting with time, with a rate of 0.0467(0.0023) MHz/min. Though the test repump powers for the acquired detuning corrections are different, there is no evidence that the pump frequency shift is related to the repump power. Considering that the time for one loading run with different test pump powers and a constant test pump detuning is 48 s, the corresponded pump laser frequency shift is 0.037 MHz, which makes small effects on the trapped atom numbers. Moreover, the frequency shift during the time of measuring all the G values in Fig. 4.1 with a fixed repump power is 0.34 MHz, it is a tiny change

that we do not need to worry about except when calculating correct values of A and B. To produce light of stable frequency to the MOT setups, the laser is locked to a frequency corresponding to the sharp edge of a transition peak in the error signal resulting from the saturated absorption spectrum. The phenomenon of the frequency shift tells that the pump frequency is gradually pushed away from the locking point due to the drift in the electronics. Nevertheless, based on the fitting result in Fig. 4.3, one can compose the actual detuning value Δ_t for each G versus P data set measured during this period using $\Delta_t = \Delta + \Delta'$.

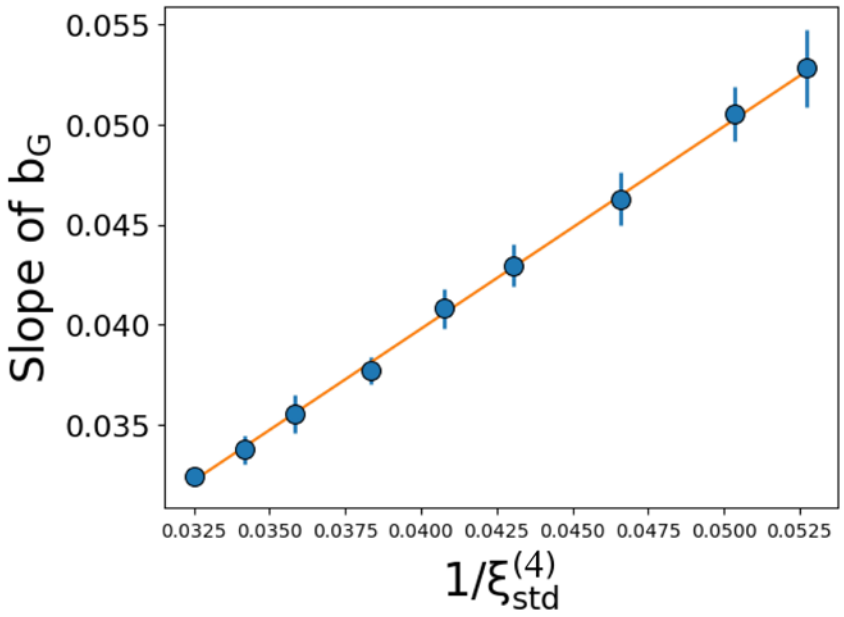

Figure 4.4: The slope of b_G versus A as a function of the simplified theoretical value of the scaling factor $1/\xi^{(4)}_{std}$. The solid straight line fits the data points linearly with an equation: y = 0.990 (0.025)x + 0.001(0.000). The slope of this equation is approximately 1, and the intercept is very close to 0, which indicates that the experimental data points accept the theoretical values very well.

To verify the validity of this detuning correction method, the common scaling factor $1/\xi^{(4)}_{std}$ was found experimentally for various standard settings by plotting the intercept b_G as a function of $A = 1 + (2\Delta_t/\gamma)^2$ and founding its slope, recalling that $b_G = A/\xi^{(4)}_{std}$ in Eq. (2.37). These measured values were plotted versus the simplified theoretical values calculated from Eq. (2.43), using the detuning correc-

tion value Δ' and the standard saturation parameter s_{sat} derived from Fig. 4.2. Fig. 4.4 displays the relationship between these two quantities, which is expected to be in direct proportion if the fitted parameters Δ' and s_{sat} are accurate. In accordance with expectations, the straight fitting line in Fig. 4.4 has a slope of approximately 1 and a negligible intercept, thus provides evidence for the precision of Δ' and s_{std} fitted from Eq. (2.44).

4.2 Measurement of Saturation Parameters

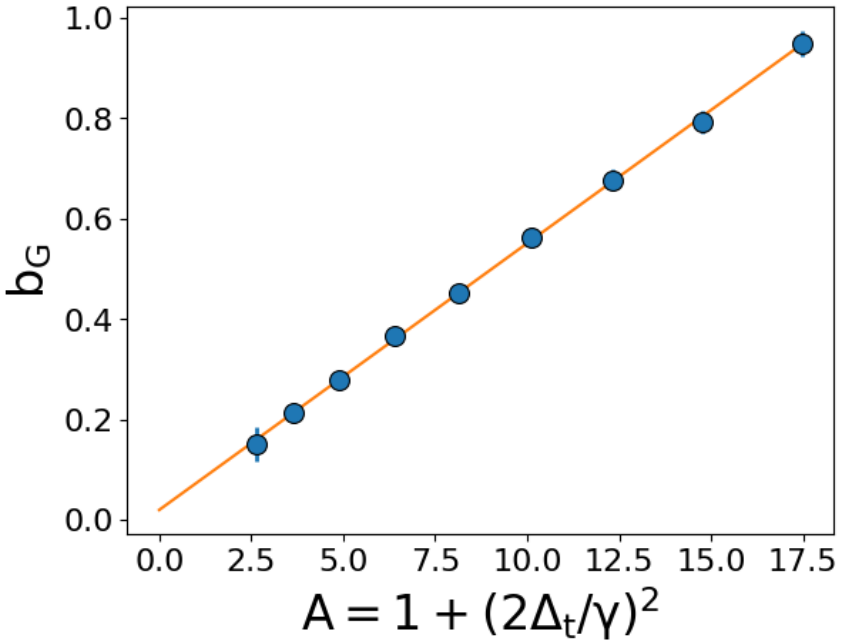

Figure 4.5: The intercepts from Fig. 4.1 as a function of the modified $A = 1 + (2\Delta_t/\gamma)^2$. A solid line fits the intercept values by a linear equation $b_G = 0.0530$ (0.0020) A + 0.0212 (0.0195), which shows a linear relationship between the two quantities as we expected in Eq. (2.37): $b_G = A/\xi^{(4)}_{\text{std}}$, and the intercept from the figure is very close to zero.

After correcting the parameters A and B using the actual detuning values Δ_t, b_G for one test repump power $P_r = 0.009$ mW is plotted in Fig. 4.5, and the intercept of b_G from Fig. 4.5 and for other repump powers are plotted as a function of the

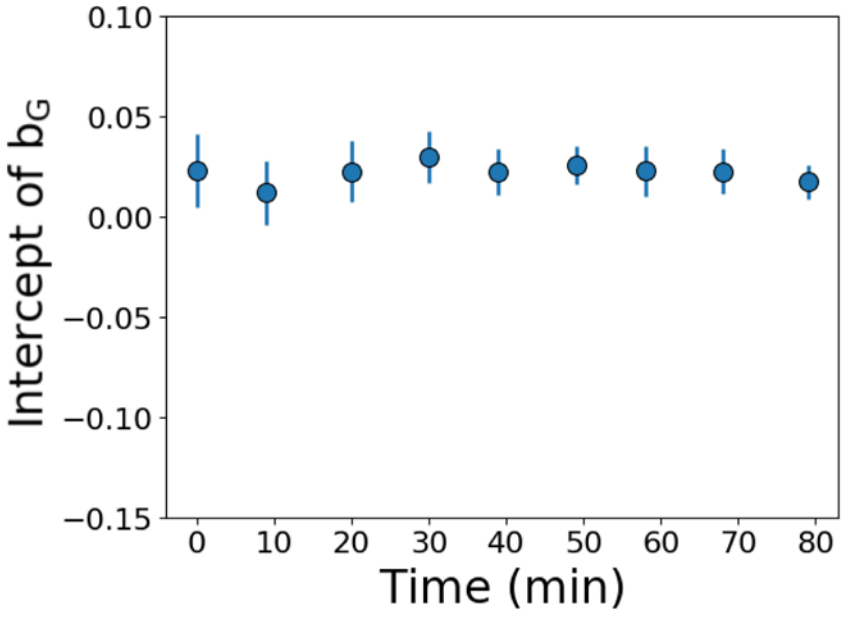

Figure 4.6: The intercept of b_G versus A as a function of the measured time. Eq. (2.37) predicts that this value is roughly equal to zero. The figure indicates that it is independent of time as we expected, but the values are slightly higher than zero.

P_r (mW)	Slope of Y (mW^{-1})	Intercept of Y (mW^{-1})	k_r	P_{sat} (mW)	$A_r P_{r,sat}$ (mW)
0.009	71.3 (55.4)	0.815 (0.083)	248(192)	1.23 (0.12)	2.21 (1.71)
0.011	51.9 (44.7)	0.840 (0.070)	176 (148)	1.19 (0.10)	1.91 (1.61)
0.013	45.4 (39.0)	0.813 (0.067)	159 (135)	1.23 (0.10)	2.05 (1.73)
0.017	50.9 (30.3)	0.779 (0.056)	186 (110)	1.28 (0.09)	3.13 (1.85)
0.023	30.6 (10.8)	0.810 (0.035)	109 (72)	1.23 (0.05)	2.46 (1.63)
0.029	17.3 (16.7)	0.826 (0.033)	61.7 (56.5)	1.21 (0.05)	1.73 (1.59)
0.037	14.3 (16.9)	0.829 (0.033)	51.2 (57.1)	1.21 (0.05)	1.82 (2.03)
0.073	-6.00 (15.5)	0.818 (0.031)	-17.5 (53.2)	1.22 (0.05)	-1.42 (4.33)
0.483	-23.4 (11.8)	0.814 (0.025)	-77.6 (40.6)	1.23 (0.04)	-38.5 (20.1)

Table 4.1: Slopes and intercepts obtained from the plots of Y versus A/B for nine different repump powers. The experimental values of k_r, P_{sat}, and $P_{r,sat}$ are composed from the measured data in the the first three columns.

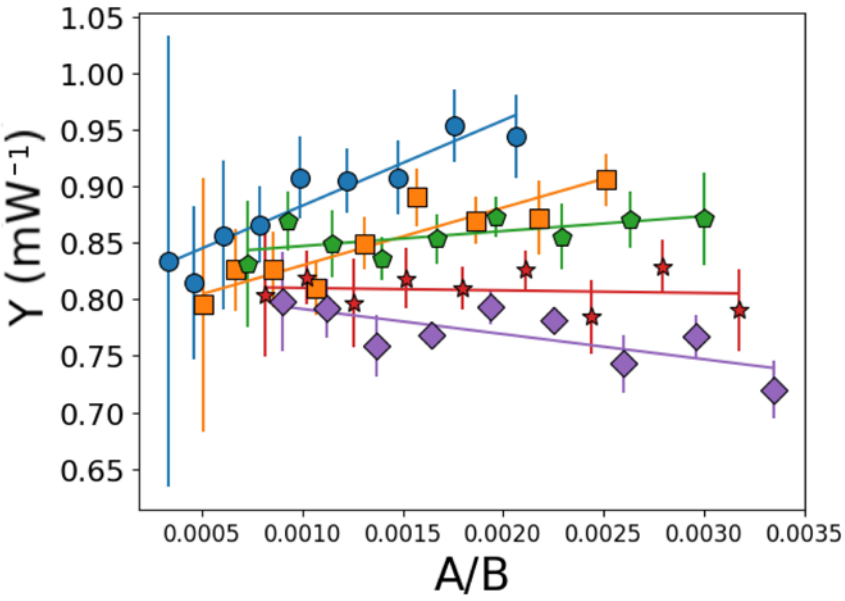

Figure 4.7: The normalized slopes $Y = m_G A/b_G$ from the plots of G versus P as a function of the modified $A/B = (\gamma^2 + 4\Delta_t^2)/[\gamma^2 + 4(\Delta_{hf} + \Delta_t)^2]$. Five sets of data points are fitted linearly to straight lines, which correspond to repump power of $P_r = 0.009$ (●), 0.017 (■), 0.037 (⬟), 0.073 (★), and 0.483 (◆) mW. The slope of these fitted lines is decreasing as the repump power increases. It agrees with our expectation in Eq. (2.38), that the increasing P_r lowers the value of k_r, and thus decreases the slope in the figure.

measured time in Fig. 4.6. Eq. (2.37) predicts that the intercept value b_G and A should be linearly related with zero intercept, which is exactly in agreement with the result in Fig. 4.5. Consistently, the intercepts of b_G for all the repump powers, shown in Fig. 4.6, present nonzero but small positive values.

Fig. 4.7 plots the normalized slopes Y for different repump powers. The linear relationship between Y and A/B also coincides with the predictions in Eq. (2.38). Furthermore, the slopes of the data points in Fig. 4.7 decrease from positive to negative, as we increase the repump power, which obeys the relationship between the slope value $\epsilon(k_r-3)/P_{sat}$ in Eq. (2.38) and the repump power $k_r = 2+P_{r,sat}/P_r$. The slopes and intercepts of Y are extracted for the saturation power calculations and listed in Table. (4.1), where the empirical pump saturation power P_{sat} and the repump effect parameter k_r are collected from Eq. (2.39): $P_{sat} = 1/F$, and Eq. (2.40): $k_r = E/(\epsilon F) + 3$, respectively.

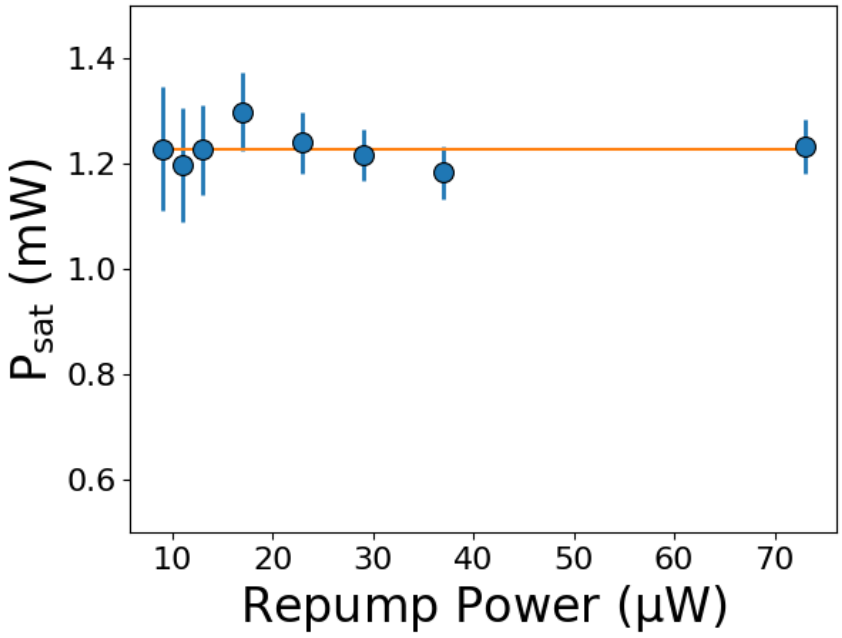

Figure 4.8: A plot of the experimental pump saturation power P_{sat} measured with different repump powers P_r. These two quantities are not related to each other as we expected. The mean value of P_{sat} is 1.23 (0.03) mW.

Fig. 4.8 displays the empirical pump saturation power for different repump powers. One can notice that the P_{sat} value is independent of P_r, which is in agree-

ment with our prediction and shows the precision of the detuning correction values. The mean value in Fig. 4.8 returns $P_{sat} = 1.23$ (0.03) mW, which falls within a reasonable range compared to the estimate discussed before (1.99 (0.74) mW).

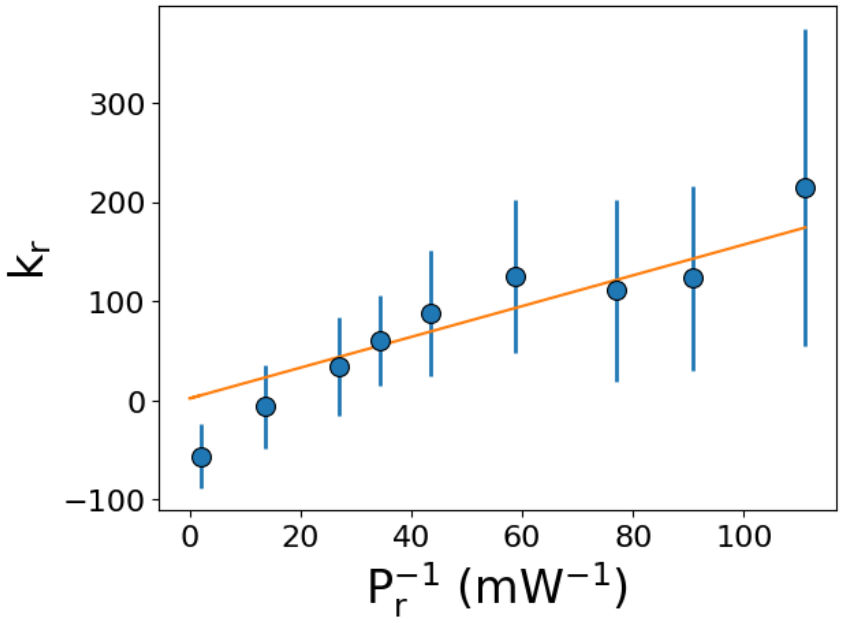

Figure 4.9: A plot of the repump parameter k_r as functions of $1/P_r$. As we expected, k_r linearly increases with $1/P_r$, but non-linearity is observed for the last 3 points. The straight line is fitting k_r and $1/P_r$ with a constrained intercept of 2, generating a result: $P_{r,sat} = 1.73$ (0.43) mW.

Moreover, The repump parameter k_r is plotted as functions of $1/P_r$ in Fig. 4.9. Recall that $k_r = 2 + P_{r,sat}/P_r$, the calculated repump effect parameter k_r is expected to be linear with the inverse of repump power $1/P_r$, with a minimum of 2. It also predicts that $k_r = 3$ when $P_r = P_{r,sat}$. Fig. 4.9 shows that k_r is linearly increasing with $1/P_r$. A straight line with a constrained intercept of 2 fits k_r as a function of $1/P_r$ in the figure. It is inside the error of all the data points, except the first one. The slope of the fitting line provides a composed repump saturation power $P_{r,sat} =$ 1.73 (0.43) mW, which is lower than the previously estimated repump saturation power (3.35 (1.25) mW). However, in Fig. 4.9 a value of $k_r = 3$ corresponds to a repump power falling between 0.037 and 0.073 mW (between the second point and the third point), this leads to a totally different result: 0.037 mW $< P_{r,sat} <$

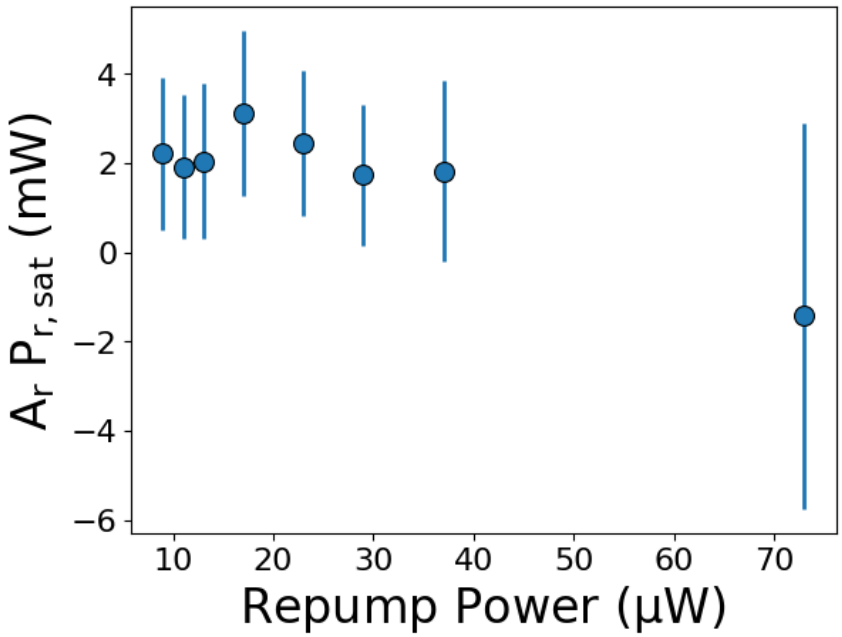

Figure 4.10: A plot of the experimental repump saturation power $P_{r,sat}$ times a detuning-related factor $A_r = 1 + (2\Delta_r/\gamma)^2$ for different repump powers. The value of $A_r P_{r,sat}$ has no significant overall changes for the first seven measured data sets and drops to a negative value after that. The average value of $A_r P_{r,sat}$ excluding the negative point is $A_r P_{r,sat} = 1.74\ (0.16)$ mW.

0.073 mW. Besides, k_r should always be positive, according to Eq. (2.27), whereas the empirical values of the first two points in the figure are negative. The first problem could be due to the shifted frequency of the repump laser. As noted in Eq. (2.45), k_r is only proportional to the inverse value of the repump power when the repump detuning is kept zero in the experiment. If the repump frequency changes, in a similar fashion of the drift in the pump laser detuning, the parameter $A_r = 1 + (2\Delta_r/\gamma)^2$ in Eq. (2.46) is no longer a constant value, which makes it hard to acquire the repump saturation power. The value of $A_r P_{r,sat}$ are calculated from Eq. (2.45) and plotted in Fig. 4.10. It is shown in the figure that the measured value of $A_r P_{r,sat}$ fluctuates around 2 mW for the repump powers below 40 μW, and drops to a negative value for higher repump powers due to the drift in the repump laser detuning. The average value of $A_r P_{r,sat}$ excluding the negative one is $A_r P_{r,sat}$ = 1.74 (0.16) mW, which agrees with the value of the slope in Fig. 4.9.

4.3 Calculation of the Excited-state Fraction

From the analysis of the repump frequency shift in section 4.2, the detuning-related parameter A_r is combined with $P_{r,sat}$ by multiplication when determining the excited-state fraction of the atoms in the MOT. Thus Eq. (2.49) becomes

$$f_e^{(4)} = \frac{s}{2\left[A\left(1 - 2\epsilon\frac{A}{B}\right) + s\left(1 + \epsilon(A_r\frac{P_{r,sat}}{P_r} - 1)\frac{A}{B}\right)\right]}. \tag{4.1}$$

Our empirical values of the saturation powers are P_{sat}=1.23 (0.03) mW and $A_r P_{r,sat}$ = 1.73 (0.43) mW. Therefore f_e can be expressed as a parameter dependent on Δ, P, and P_r:

$$f_e^{(4)} = \frac{P/(1.23\text{ mW})}{2\left[A\left(1-(2\times0.357)\frac{A}{B}\right)+(P/(1.23\text{ mW}))\left(1+0.357((1.73\text{ mW})/\mathrm{P_r}-1)\frac{\mathrm{A}}{\mathrm{B}}\right)\right]}, \tag{4.2}$$

while in the two-level model $f_e^{(2)}$ is only related to Δ and P:

$$f_e^{(2)} = \frac{P/(1.23\text{ mW})}{2(A + P/(1.23\text{ mW}))}. \tag{4.3}$$

The values of the excited-state fractions in the two-level model and the four-level model are plotted as a function of the repump laser power in Fig. 4.11. $f_e^{(2)}$ remains constant in this figure, since the effect of the repump transition is not taken into account in this model. For comparison, $f_e^{(4)}$ starts from zero when the repump power is zero, which is more reasonable than the two-level model. It then quickly

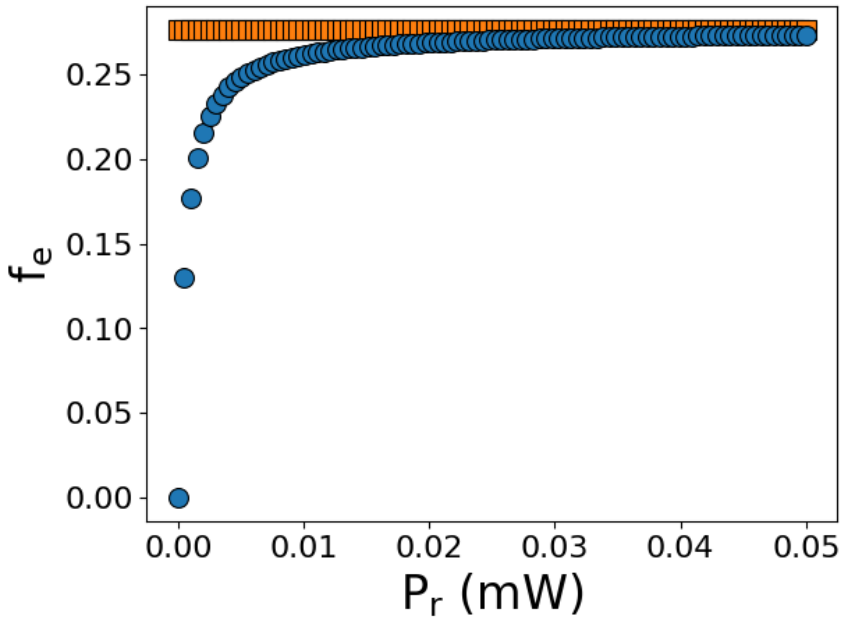

Figure 4.11: A plot of the determined excite-state fraction in the two-level model (■) and the four-level model (●) for different repump powers. Here Δ=-10 MHz and P=18 mW. As P_r increases, $f_e^{(2)}$ remains constant while $f_e^{(4)}$ increases from zero to the same level as $f_e^{(2)}$.

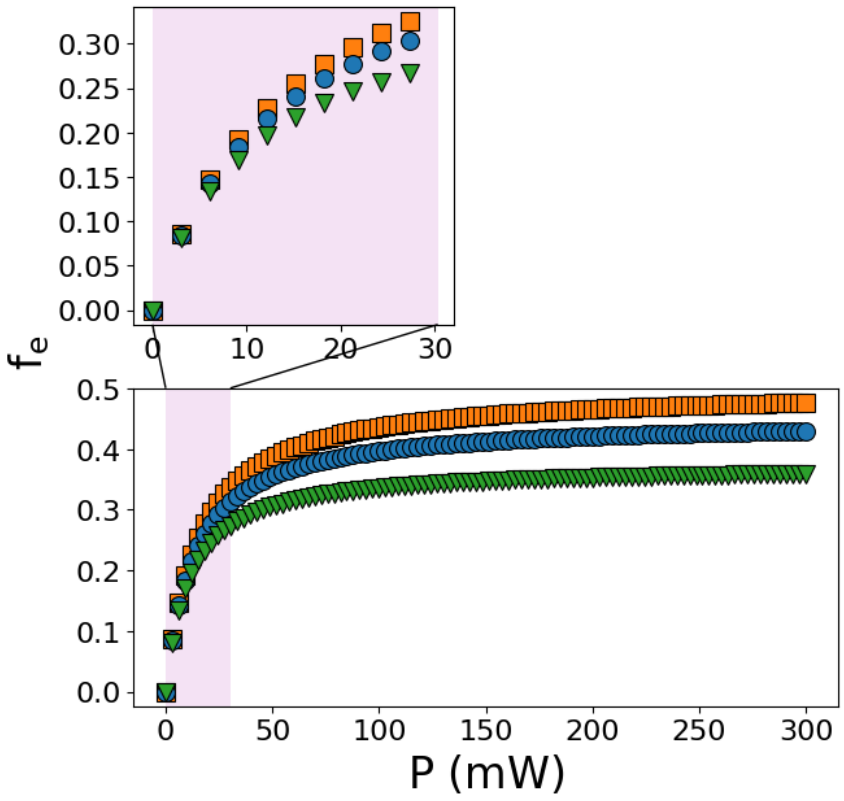

Figure 4.12: A plot of the determined excite-state fraction in the two-level model (■), the four-level model with P_r=0.009 mW (●), and the four-level model with P_r=0.003 mW (▼) for different pump powers. Here Δ=-10 MHz. These three curves saturate at different levels, since the atoms are spending less time in the dark state with a higher repump power. The inset figure shows a 20% discrepancy between $f_e^{(2)}$ (■) and $f_e^{(4)}$ with P_r=0.003 mW (▼) when P=28 mW.

increases and reaches the same level as the two-level model, since the atoms are quickly transferred from the dark state to the excited state with a high repump power.

We can also plot the excited-fraction as a function of the pump laser power in Fig. 4.12 with $\Delta = -10MHz$. The three curves shown in the figure represent the excited-state fractions with different repump powers ($f_e^{(2)}$, $f_e^{(4)}$ with P_r=0.003 mW, $f_e^{(4)}$ with P_r=0.009 mW). They are all increasing as the pump power increases since more atoms are transferred to the excited-state, and they saturate at different levels as P goes to infinity, which is due to the accumulated atoms in the dark state controlled by the repump transition. In the range of the pump power that we can reach in the experiment, there is a 20% discrepancy between $f_e^{(2)}$ and $f_e^{(4)}$ with P_r=0.003 mW. It is not a big difference, but considering that the excited-state loss coefficient $< \sigma v >*$ is large compared to the the ground-state loss coefficient, an accurate excited-state fraction value is required.

For comparison, Shah *et al*. [**?**] model-independently measured the excited fraction of ^{87}Rb atoms trapped in a MOT using a charge transfer technique, and built a model which accurately estimates f_e with the knowledge of only the pump laser intensity and detuning. It is not surprising that Shah proposed that P and Δ are dominant factors for f_e, since repump transition becomes more significant when it is very weak. Therefore, we can conclude that the four-level atomic model is reliable for the excited-state fraction, especially when the repump power is small.

4.4 Hypothesis of Atom Pinning for High Laser Power

In Section 4.1 we have discussed the behaviour of G as a function of the test pump power, which is quite linear as we expected. However, there is also a tendency that G is going to saturate as the pump power decreases. It is more obvious in Fig. 4.13 where G values with lower pump powers are plotted. The value of G with high pump power is fitted linearly, which is shown by the solid straight lines in Fig. 4.13, and the residuals of G are plotted in Fig. 4.14. When the pump detuning is smaller than -10 MHz, the residuals of G are independent of P, with a constant value of approximately zero. But for a further detuned pump laser light, the residuals increase dramatically as the pump power decreases, especially when Δ=-14 MHz. One hypothesis that can explain this phenomenon is that the atoms in the cycling transition can be seen as in small lattices. The trap depth of the atom, which is the energy required to remove the atom from the trap, is proportional to the laser power and inversely proportional to the laser detuning squared: $U_{trap} \propto P/\Delta^2$ [**?**]. Therefore, for large pump power and small pump detuning, the depth of the lattice is high, which means the atoms may not be easily transferred to other states and can be pinned on certain transitions, corresponding to a lower saturation intensity. For

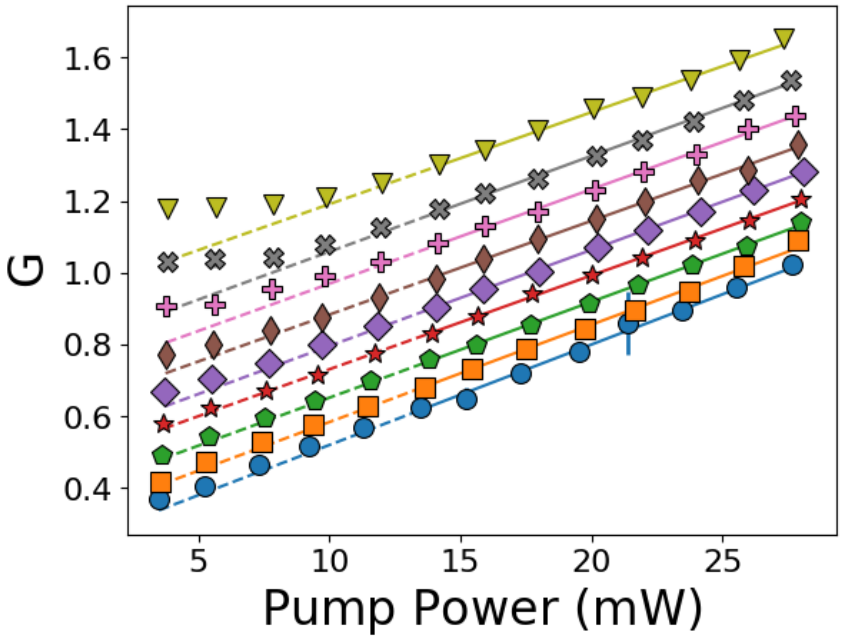

Figure 4.13: A plot of G versus the test setting pump power P. The last 8 points in each set of data are fitted to a line and corresponds to pump laser detunings of $\Delta/2\pi$ = -6 (●), -7 (■), -8 (⬟), -9 (★), -10 (◆), -11 (♦), -12 (✚), -13 (✖), and -14 (▼) MHz. Here P_r=0.483 mW.

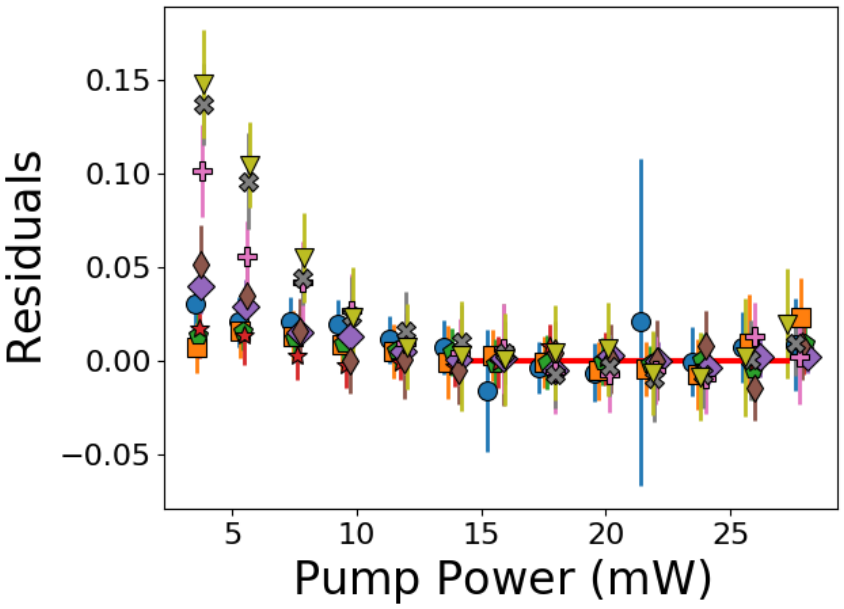

Figure 4.14: Residuals of G from the linear fittings in Fig. 4.13. Each data set corresponds to a pump laser detuning of $\Delta/2\pi$ = -6 (●), -7 (■), -8 (⬟), -9 (★), -10 (◆), -11 (♦), -12 (✚), -13 (✖), and -14 (▼) MHz.

example, the saturation intensity for the $|F = 2, m_F = \pm 2\rangle \rightarrow |F = 3, m'_F = \pm 3\rangle$ transition is $I_{sat(m_F=\pm 2 \rightarrow m'_F=\pm 3)} = 1.669\ \mathrm{mW/cm^2}$ [**?**], which is lower than the averaged pump saturation intensity $I_{sat} = 3.577\ \mathrm{mW/cm^2}$, and the corresponding estimated saturation power is $P_{sat(m_F=\pm 2 \rightarrow m'_F=\pm 3)} = 1.39\ (0.52)$ mW.

Detuning (MHz)	A	Slope ($\mathrm{mW^{-1}}$)	Intercept
-6	4.91	0.0280 (0.0006)	0.240 (0.011)
-7	6.33	0.0271 (0.0006)	0.312 (0.012)
-8	7.96	0.0268 (0.0003)	0.384 (0.007)
-9	9.81	0.0262 (0.0003)	0.469 (0.007)
-10	11.9	0.0268 (0.0002)	0.528 (0.004)
-11	14.2	0.0261 (0.0006)	0.622 (0.014)
-12	16.7	0.0263 (0.0007)	0.706 (0.015)
-13	19.4	0.0267 (0.0006)	0.791 (0.013)
-14	22.3	0.0256 (0.0008)	0.935 (0.017)

Table 4.2: Slopes and intercepts obtained from the fitting lines for high power in Fig. 4.13 when $P_r = 0.483$ mW.

The slopes and intercepts from the high-power fits in Fig. 4.13 are listed in Table. 4.2, where the slopes are all about the same value, and the intercepts are proportional to A. Assuming that the atom pinning hypothesis is true, the saturation parameters P_{sat} and k_r can be extracted using the same method in Section 4.2, but only from the measured G values for high pump power (13 mW to 28 mW). Fig. 4.15 shows the calculated pump saturation powers for different repump powers. The result gives an average value of $P_{sat} = 1.15\ (0.06)$ mW, which is in the range of the estimated saturation power for the $\sigma^{\pm}$ transitions (1.39 (0.52) mW). Moreover, the relationship between the repump effect parameter k_r and $1/P_r$ is plotted in Fig. 4.16, where a straight line with a constrained intercept of 2 is fitting k_r as a function of $1/P_r$. This figure is more reasonable than Fig. 4.9, since the fitting line falls inside all the data points, and its slope provides $P_{r,sat} = 2.05\ (0.59)$ mW. Hence, it is possible that the saturation parameters are not constants, but can change with the laser conditions. That makes our model more complicated and requires more calculations in the next steps.

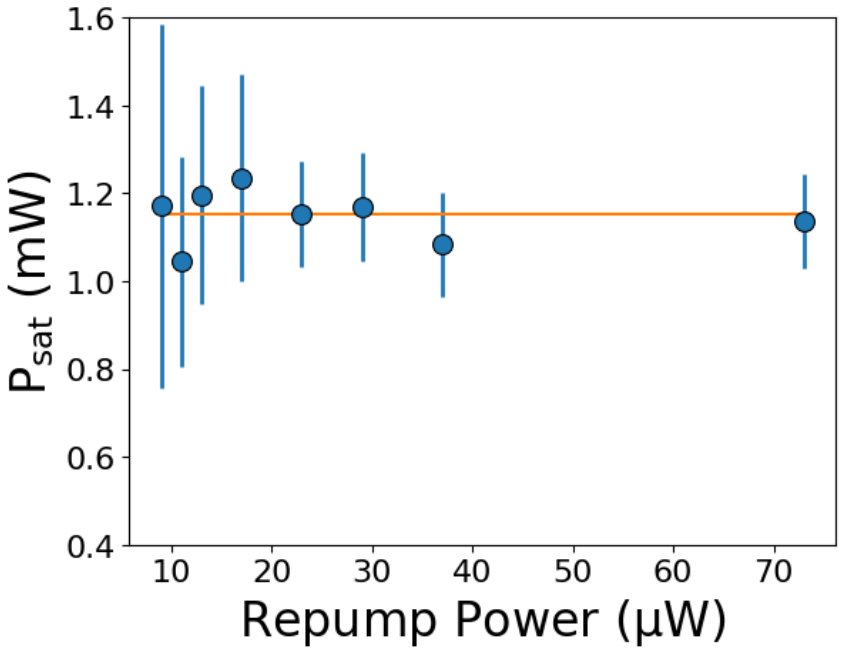

Figure 4.15: A plot of the experimental pump saturation power P_{sat} for different repump powers. The data gives a mean value of $P_{\text{sat}} = 1.15\ (0.06)$ mW.

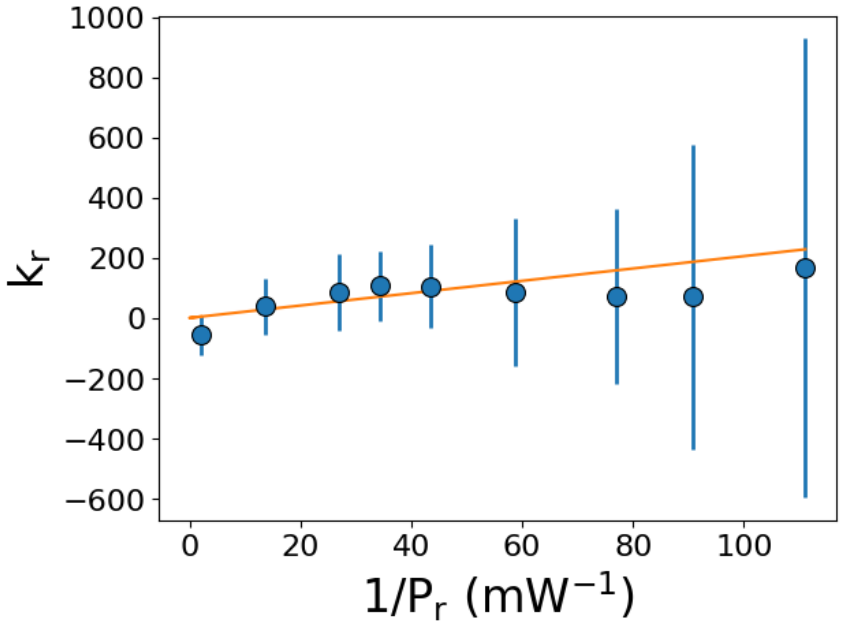

Figure 4.16: A plot of the repump parameter k_r as functions of $1/P_r$. The straight line is fitting k_r and k_r with a constrained intercept of 2, which gives $P_{r,sat} = 2.05$ (0.59) mW.

Chapter 5

Conclusion

5.1 Summary

In this work we have demonstrated a simple method to experimentally determine and control the excited-state fraction of the atoms in a MOT. A four-level theoretical atomic model was used to describe the transitions of the atoms in a MOT, and an experimental parameter G is constructed and measured to determine the saturation parameters for the pump ($F = 2 \rightarrow F = 3'$) and repump ($F = 1 \rightarrow F = 2'$) transitions in D_2 line ($5^2S_{1/2} \rightarrow 5^2P_{3/2}$) for ^{87}Rb. By fitting the intercept of G versus P, b_{G}, we successfully measured the accurate pump laser frequency, therefore deduced a reliable pump saturation power with precision (P_{sat}=1.23 (0.03) mW). However, because of the unknown frequency shift of the repump laser, only a product of the repump saturation power times a detuning-related factor is measured: $A_{\mathrm{r}}P_{\mathrm{r,sat}} =$ 1.73 (0.43) mW.

The excited-state fraction f_{e} can be calculated from these two measured saturation parameters for different laser powers and detunings. The two-level model prediction is independent of the repump laser power being used. However, it shows that the four-level model better explains the measured result, and gives a wider range of the excited-state fractions. For the experimental settings currently available, a range of the excited state fractions from 0.045 to 0.415 can be achieved.

5.2 Future Work

In the next step, we can apply the determination of the excited-state fraction to measurements of the trap loss rates while keeping the trap depth constant, since the loss rate coefficient is dependent on the trap depth. Fig. 5.1 predicts the relationship between the loss rate of the atoms in the MOT, Γ, and the excited-state fraction, f_{e}. When $f_{\mathrm{e}} = 1$, which means that all the atoms are in the excited state, the measured trap loss is only due to the excited-state collisions $n_{\mathrm{Rb}} < \sigma v >_{\mathrm{Rb+Rb*}}$. Similarly, when $f_{\mathrm{e}} = 0$, Γ is related to the ground-state cross section $n_{\mathrm{Rb}} < \sigma v >_{\mathrm{Rb+Rb}}$. One challenge in this measurement is to determine different excited-state fractions with the same trap depth, which needs to be modelled and tested.

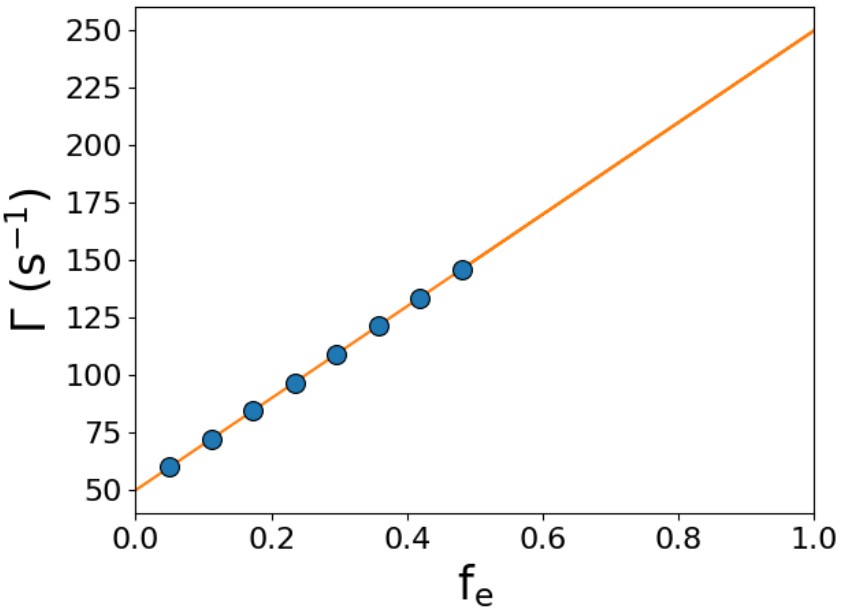

Figure 5.1: A plot of the trap loss rate from the MOT as a function of the excited-state fraction with a constant trap depth. The extrapolation of Γ from f_e=0 and f_e=1 indicate the ground-state cross section and the excited-state cross section for one trap depth, respectively.

Moreover, we can control the trap depth by varying the size of the laser beams and make the same measurement. The laser intensity should be kept constant, which also indicates a constant excited-state fraction. Such experiments will lead to a direct measurement of the excited-state cross sections. The result of particular interest is the measurement of the ^{87}Rb hitting ^{87}Rb atoms in their excited state, which can be distinguished from the collisions of ^{85}Rb hitting ^{87}Rb atoms in their excited state. This will provide a first measurement distinguishing between isotopic collision partners.

Appendix A

Data and code address

The experimental data is stored in the following address: C:\Users\QDG\repo\QDG-bus-v1\BCodeGen for TD\MOT_Data\Yue_document\G_values_with_different_repump_powers_24.04.18.

The experimental driving and analysis codes written in Python 3 are located in: C:\Users\QDG\repo\QDG-bus-v1\BCodeGen for TD. The names and functions of the codes are:

- **main_code.py**: run and control the measurement of the scattered light and the MOT fluorescence for one repump power.
- **Analysis_main.py**: extract the determined voltages by fitting the fluorescence data.
- **Analysis_class.py**: define some classes used in Analysis_main.py.
- **G_parameter_different_repump_power.py**: use the values of G measured in Analysis_main.py to calculate the saturation parameters.
- **DefaultSettings.py**: a dictionary of the controllable settings used in the measurement, the settings can also be reedited in the above scripts.